Univerzita Karlova
Prírodovedecká fakulta

Študijný program: Chémia
Študijný obor: Chémia

Samuel Kolesár

Syntéza zeolitom-stabilizovaných bimetalických nanočastíc na valorizáciu lignínu
Synthesis of zeolite-supported bimetallic nanoparticles for lignin valorisation

Bakalárska práca

Školiteľ: Mgr. Michal Mazur, Ph.D.
Konzultant: Paul A. Diddams, Ph.D.

Praha, 2025

Charles University
Faculty of Science

Study programme: Chemistry
Branch of study: Chemistry

Samuel Kolesár

Synthesis of zeolite-supported bimetallic nanoparticles for lignin valorisation
Syntéza zeolitom-stabilizovaných bimetalických nanočastíc na valorizáciu lignínu

Bachelor's thesis

Supervisor: Mgr. Michal Mazur, Ph.D.
Consultant: Paul A. Diddams, Ph.D.

Prague, 2025

Prehlásenie

Prehlasujem, že som túto záverečnú prácu spracoval samostatne, a že som uviedol všetky použité informačné zdroje a literatúru. Ďalej prehlasujem, že táto práca a ani jej podstatná časť nebola predložená k získaniu iného alebo rovnakého akademického titulu.

V Prahe, 12.05.2025 Samuel Kolesár

Abstract

Lignin is a complex natural polymer constituting a part of plant cell walls. Despite the accessibility and renewability of this feedstock, it remains vastly underexploited, primarily serving as combustion waste fuel. However, its high aromatic content positions it as a promising resource of high-value aromatic compounds. The application of metal nanoparticles (NPs) anchored to zeolites in lignin valorisation offers new economic and ecological opportunities. The thesis primarily focused on mechanochemical stabilisation of mono- and bimetallic NPs at zeolitic supports. Prepared catalysts were tested in the hydrogenation reaction of the lignin model compound, i.e., eugenol.

Herein, I synthesised a gallosilicate MFI nanosponge, modified it, and utilised it as a support for metal NPs. The support was obtained *via* a hydrothermal synthesis. Nanosponge architecture featured an interconnected, disordered network of MFI nanolayers. The following degallation of the zeolite, by concentrated nitric acid, generated silanol nests. These nests further served as molecular anchors, greatly enhancing the material's capacity for metal NPs immobilisation. Nanoparticles were introduced by post-synthesis mechanochemical wet impregnation of metals (Pt, Pd, Rh, Ru, Ni, and Cu). Moreover, Pt and Pd species were prepared in the form of bimetallic nanoparticles by co-impregnation with RE elements (La, Ce, or Y). Materials were comprehensively characterised using PXRD, N_2 sorption, and SEM, followed by detailed STEM and EDS analysis, to evaluate metal particle size and dispersion. Simultaneous incorporation of RE elements alongside primary metal species yielded more sintering-resistant, and smaller NPs (1.1–1.4 nm, in size) compared to monometallic samples (1.4–2.0 nm).

The catalytic performance of the materials was assessed by the selective hydrogenation and hydrodeoxygenation (HDO) of eugenol. Hydrogenation was conducted for over 6 h at the H_2 pressure of 25 bars at 150 °C. Catalysts demonstrated high activity (conversions in the range of 53–100 %), with hydrogenation of the eugenol terminal double bond being a dominant process. Formation of variously hydrogenated and HDO products was observed, although the yields of HDO compounds remained low (<0.5–7 %). The highest HDO activity was observed for the Ru catalyst, highlighting Ru's strong oxygen-binding affinity. Moreover, the incorporation of RE elements as

metal promoters amplified the HDO product formation, suggesting their auspicious application in eugenol HDO. Overall, this thesis allowed in-depth investigation of metal-support interactions and catalytic performance of such materials.

Key words:

Zeolites; hydrothermal synthesis; mechanochemistry; bimetallic nanoparticles; rare-earth elements; electron microscopy; lignin valorisation; eugenol

Abstrakt

Lignín je komplexný prírodný polymér tvoriaci časť bunkových stien rastlín. Napriek dostupnosti a obnoviteľnosti tejto suroviny zostáva lignín výrazne nevyužitý, primárne slúžiaci ako odpadové palivo na spaľovanie. Jeho vysoký obsah aromatických zlúčenín ho však radí medzi sľubné zdroje cenných aromatických látok. Využitie zeolitom-stabilizovaných kovových nanočastíc na valorizáciu lignínu ponúka nové ekonomické a ekologické možnosti. Táto práca bola primárne zameraná na mechanochemickú stabilizáciu mono- a bimetalických nanočastíc na zeolitových nosičoch. Pripravené katalyzátory boli testované v hydrogenačnej reakcii modelovej zlúčeniny lignínu, teda eugenolu.

V tejto práci som syntetizoval galosilikátový MFI nanosponge, modifikoval ho a využil ako nosič pre kovové nanočastice. Nosič bol pripravený hydrotermálnou syntézou. Nanosponge architektúra zahŕňala prepojenú, neusporiadanú sieť MFI nanovrstiev. Následná degalácia zeolitu koncentrovanou kyselinou dusičnou vytvorila silanolové hniezda. Tieto hniezda ďalej slúžili ako molekulárne kotvy, čím výrazne zvyšovali schopnosť materiálu imobilizovať kovové nanočastice. Nanočastice boli zavedené post-syntetickou mechanochemickou impregnáciou kovov (Pt, Pd, Rh, Ru, Ni a Cu) mokrou cestou. Okrem toho boli častice Pt a Pd pripravené vo forme bimetalických nanočastíc pomocou koimpregnácie s prvkami vzácnych zemín (La, Ce alebo Y). Materiály boli komplexne charakterizované pomocou PXRD, N_2 sorpcie a SEM, nasledované detailnou STEM a EDS analýzou za účelom vyhodnotenia veľkosti a disperzie kovových častíc. Simultánna inkorporácia prvkov vzácnych zemín spolu s primárnymi kovmi viedla k tvorbe menších nanočastíc (1,1–1,4 nm) odolnejších voči spekaniu v porovnaní s monometalickými vzorkami (1,4–2,0 nm).

Katalytické vlastnosti materiálov boli hodnotené v procese selektívnej hydrogenácie a hydrodeoxygenácie (HDO) eugenolu. Hydrogenácia prebiehala po dobu 6 hodín pri tlaku H_2 25 barov a teplote 150 °C. Katalyzátory preukázali vysokú aktivitu (konverzie v intervale 53–100 %), pričom ale dominantným procesom bola hydrogenácia koncovej dvojnej väzby eugenolu. Bola pozorovaná tvorba rôzne hydrogenovaných a HDO produktov, pričom výťažky HDO zlúčenín zostali nízke (<0.5–7 %). Najvyššia HDO aktivita bola zaznamenaná v prípade Ru katalyzátoru, čo poukazuje na jeho silnú afinitu ku kyslíku. Okrem toho, inkorporácia prvkov vzácnych zemín ako kovových

promotérov zvýšila tvorbu HDO produktov, čo naznačuje ich potenciálne budúce využitie na HDO eugenolu. Táto práca celkovo poskytla podrobný pohľad na interakcie medzi kovom a nosičom, a zároveň na katalytické vlastnosti týchto materiálov.

Kľúčové slová:

Zeolity; hydrotermálna syntéza; mechanochémia; bimetalické nanočastice; prvky vzácnych zemín; elektrónová mikroskopia; valorizáciu lignínu; eugenol

Acknowledgement

First and foremost, I am immensely grateful to my supervisor, Mgr. Michal Mazur, Ph.D., for his invaluable guidance, constructive feedback, continuous encouragement and patience. Many thanks belong to my consultant, Paul Diddams, Ph.D., for his industrial expertise and insights that have been instrumental in shaping this research. I would also like to extend my sincere appreciation to all members of Prof. Jiří Čejka's group of Heterogeneous Catalysis and Advanced Materials, especially Ing. Jan Přech, Ph.D., for his valuable advice in the field of catalysis; Ing. Martin Kubů, Ph.D., for his help with N_2 sorption measurements; and to Mgr. Monika Remzová, Ph.D., and Mgr. Anna Laštovičková for their assistance with SEM and STEM measurements. Finally, I am greatly thankful to those who contributed directly or indirectly to this study, through insightful discussions, resources, or moral support.

List of abbreviations

3D	Three-dimensional
ABF	Annular bright-field
ADF	Annular dark-field
BET	Brunauer-Emmet-Teller
BSE	Backscattered electrons
EDS	Energy-dispersive X-ray spectroscopy
EELS	Electron energy loss spectroscopy
EUG	Eugenol
FCC	Fluid catalytic cracking
FID	Flame ionisation detector
GC	Gas chromatography
HAADF-STEM	High-angle annular dark-field scanning transmission electron microscopy
HDO	Hydrodeoxygenation
HT-GC	High temperature gas chromatography
iEUG	Isoeugenol
IUPAC	International Union on Pure and Applied Chemistry
IZA-SC	Structure Commission of the Internation Zeolite Association
MFI	Zeolite topology
MFI-deGa-as	Degallated MFI nanosponge as synthesised
MFI-deGa-calc	Degallated MFI nanosponge calcined
MFI-Ga-as	Gallosilicate MFI nanosponge as synthesised
MFI-Ga-calc	Gallosilicate MFI nanosponge calcined
MPCHO	2-methoxy-4-propylcyclohexanone
MPCHOL	2-methoxy-4-propylcyclohexanol
MPPOL	2-methoxy-4-propylphenol
MS	Mass spectrometry
NPs	Nanoparticles
Pd(-RE)@MFI	Degallated MFI nanosponge impregnated with Pd metal nanoparticles (optionally with a specific rare-earth element)
PGM	Platinum group metals
PCHO	4-propylcyclohexanone

PCHOL	4-propylcyclohexanol
PPOL	4-propylphenol
PSD	Particle size distribution
Pt(-RE)@MFI	Degallated MFI nanosponge impregnated with Pt metal nanoparticles (optionally with a specific rare-earth element)
Pt@MFI-BM	Degallated MFI nanosponge impregnated with Pt metal nanoparticles (0.5 wt.%) mechanochemically by ball milling
Pt@MFI-MAN	Degallated MFI nanosponge impregnated with Pt metal nanoparticles (0.5 wt.%) by manual wet impregnation
PTFE	Polytetrafluorethylene
PXRD	Powder X-ray diffraction
RE	Rare-earth
ref	Reference
SAC	Single atom catalysts
SDA	Structure directing agent
SE	Secondary electrons
SEM	Scanning electron microscopy/microscope
SF	Solvent-free
STEM	Scanning transmission electron microscopy/microscope
TCD	Thermal conductivity detector
TEM	Transmission electron microscopy/microscope
TM	Transition metals
TPR	Temperature-programmed reduction
X(-RE)@MFI	Degallated MFI nanosponge impregnated with X metal nanoparticles (optionally with a specific rare-earth element)
ZSM-5	Zeolite Socony Mobil No. Five, type of material

Contents

1 Introduction

Lignin, a major component of plant cell walls, is currently underutilised as a feedstock, primarily serving as combustion waste fuel.[1] In addition, lignin represents one of the main undesired constituents of the pulping process. Over the past few decades, research on lignin valorisation has advanced, primarily focusing on biofuels and chemicals as crucial alternatives to petroleum-based counterparts. Its high aromatic content makes it a promising renewable source of valuable compounds with a retained aromaticity.[2] The catalytic utilisation of metal nanoparticles supported at zeolites represents one of the important approaches currently being studied for valorising lignin-derived molecules into value-added chemicals.

Zeolites are microporous crystalline elementosilicates that can be found in nature or synthesised in a laboratory. Their chemical structure comprises three-dimensional frameworks of corner-sharing TO_4 tetrahedra where T represents a central atom, such as Si, Al, Ge, Ga, etc, tetrahedrally coordinated by O atoms.[3] These materials possess properties desirable for catalysts such as a high surface area, tuneable pore structure, adjustable architecture, and high thermal and chemical stability. In addition, incorporation and stabilisation of metals as uniformly dispersed small nanoparticles in zeolites with their favourable, low mass-to-surface ratio makes such nanocomposites valuable and cost-effective catalysts, enabling us to exploit their large catalytically active surface with high efficiency.

In this work, an MFI gallosilicate of nanosponge architecture was hydrothermally synthesised. The architecture is comprised of an interconnected, disordered network of MFI nanolayers that has an immense potential as a support for metal nanoparticles. This material was degallated using concentrated nitric acid, thereby creating accessible silanol nests (surface hydroxyl groups) capable of anchoring and interacting with incorporated metal nanoparticles.[4] As a result, degallated MFI nanosponge zeolite can be used to support and immobilise various metal species. Moreover, in this work, a relatively new method was applied for post-synthesis impregnation of zeolites with metal species – wet impregnation *via* mechanochemical approach with the use of ball milling.[5,6] In this way, various combinations of mono- and bimetallic species of Pt, Pd, Rh, Ru, Ni, and Cu, and rare-earth elements i.e., La, Ce, and Y, anchored at zeolites were prepared. Incorporation of rare-earth elements is known to stabilise certain metals

in the form of smaller nanoclusters with better dispersion throughout zeolite in comparison to monometallic counterparts.[7]

Degallated MFI nanosponge support was characterised using powder X-ray diffraction. Its textural properties and porous system were examined through N_2 sorption. Electron microscopy and elemental mapping (EDS) were employed to analyse the size, location and distribution of nanoparticles in the prepared nanocomposites.

The catalytic performance of prepared materials containing various metal nanoparticles were screened using the eugenol hydrogenation reaction. Eugenol was selected as a model molecule for lignin valorisation due to its structural resemblance to the chemical structure of the building units of inconsistently composed biopolymer lignin.[2] Moreover, the eugenol molecule can undergo hydrogenation and hydrodeoxygenation reactions leading to a wide range of products[8], such as hydrogenated (e.g., 2-methoxy--4-propylphenol, 2-methoxy-4-propylcyclohexanol, etc.), or even hydrodeoxygenated products (e.g., 4-propylphenol, 4-propylcyclohexanol, etc.). Hence, the influence of the types of metals present on the extent and selectivity of eugenol conversion was monitored.

The aims of the presented bachelor thesis were:

- To develop a novel class of heterogeneous catalysts for lignin valorisation; by utilising zeolite-supported metal nanoparticles to catalyse eugenol hydrogenation as a model reaction for investigation of their catalytic performance.
- To stabilise uniformly-dispersed metal nanoparticles on zeolite MFI nanosponge; by wet impregnation employing a mechanochemical approach.
- To provide extensive insights into metal-support interactions; by thorough characterisation of prepared nanocomposites by electron microscopy.
- To describe the functionalities of various metal nanoparticles and assess their influence on selectivity towards hydrodeoxygenation in the eugenol conversion; by a screening of the catalytic performance of prepared materials.

2 Theoretical part

2.1 Zeolites

A history of zeolites started in 1756 with the discovery of these minerals by Swedish mineralogist A. F. Cronstedt. He coined the term "zeolite" which came from the Greek words *ζέω* (zeo) – to boil, and *λίθος* (lithos) – stone. This term described the observed phenomenon of the apparent boiling of the stone and the release of water upon direct heating. An eminent advancement in zeolite studies occurred in 1930 after the resolution of their crystal structures.[9] Today, more than 250 types of distinct frameworks of zeolites are recognised by the Structure Commission of the International Zeolite Association (IZA-SC) and each of them has been assigned a three-letter code.[10]

Zeolites are structurally microporous crystalline aluminosilicates, found in nature or synthesised in laboratories. Their structures consist of three-dimensional frameworks of corner-sharing SiO_4 and AlO_4 tetrahedra *via* the atom of oxygen forming an oxygen bridge (Figure 1). The length of the Si–O bond varies approximately between 1.59–1.61 Å while the value of the Al–O bond length is around 1.74 Å. For a more precise description of the structural features of zeolites, researchers came up with higher-order schemes and groupings that replace primary units – tetrahedra. The most common representatives of higher-order schemes are so-called secondary building units, composite building units and natural tiles.[3] The composition of zeolites is not limited to Si and Al, many other so-called "heteroatoms" are found in zeolite structures, e.g., Ge, Ti, Ga, B, Fe, Zr, etc. Due to the tetrahedral coordination of these elements by 4 oxygen atoms, they are commonly called T-atoms. Therefore, "elementosilicates" represent a broader term for zeolite description compared to aluminosilicates.[3,11]

The description of the pore system of zeolites classified by the number of T-atoms forming the pore opening is an important zeolite characteristic.[3] Zeolites are accordingly divided into small pore zeolites – 8 T-atoms assembling the pore ring (diameter of *ca.* 4 Å), medium pore zeolites – 10 T-atoms assembling the ring (diameter of *ca.* 5.5 Å), large pore zeolites – with 12 T-atoms (ring diameter of *ca.* 7.5 Å), and extra-large pore zeolites with 14 or more T-atoms (ring diameter over *ca.* 8 Å).[12] The size of these pore openings can be controlled during the hydrothermal synthesis of zeolites using structure directing agents (SDAs). These organic molecules influence gelation/nucleation processes when TO_4 tetrahedra are organised in a particular

geometry around organic molecules. At the final stage of zeolite synthesis, SDAs are eliminated *via* calcination at high temperatures.[13]

Insertion of heteroatoms into zeolite frameworks alters the properties of zeolites. In the case of aluminosilicates and gallosilicates, Al or Ga (trivalent) atoms inserted into the zeolite structure in place of Si (tetravalent) atoms introduce a negative charge into the framework that must be charge-balanced with extra-framework cations such as H^+, Na^+, K^+, Ca^{2+}, Mg^{2+}, etc. Brønsted acid sites arise where the extra-framework cations are exchanged for H^+. Isomorphous substitution of Si atoms in a zeolite framework for Al, Ga creates Lewis acid sites (Figure 1). The Brønsted and Lewis acidity of zeolites plays a key role in many of their catalytic applications, such as cracking and isomerisation reactions.[3,14]

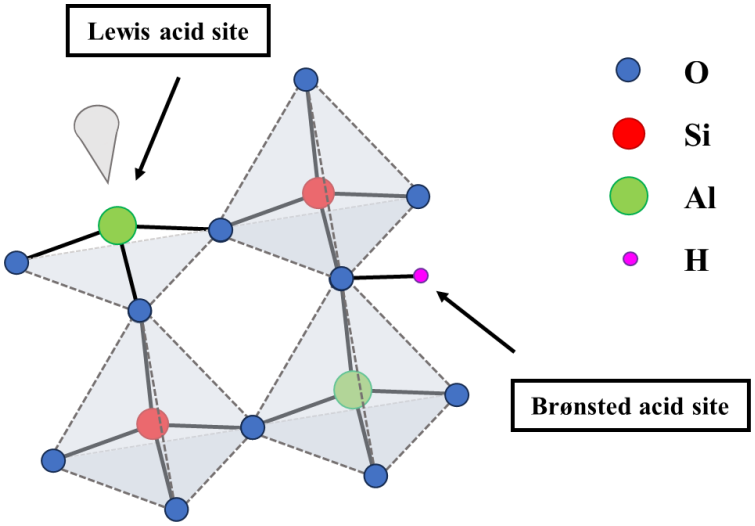

Figure 1. Illustration of zeolite framework composed of corner-sharing SiO_4 and AlO_4 tetrahedra

Zeolites are widely established as highly effective catalysts due to their remarkable thermal and chemical stability, well-defined pore system and high surface area. In addition, their tuneable acidity and unique shape-selectivity (ability to catalyse reactions based on the molecular size and shape of substrate and product molecules due to the well-defined pore architecture of zeolites) facilitate precise control over the catalytic processes. Moreover, the presence of the mentioned Brønsted and Lewis acid sites enables zeolites to act as solid acid catalysts in various organic transformations and processes, replacing conventional homogeneous acid solutions.[15,16]

These elementosilicates also represent an excellent option for supporting and stabilising metal nanoparticles. The zeolite framework influences their stabilisation through strong

metal-support interactions, controlled dispersion, confinement and electronic effects. Effective stabilisation inhibits or prevents aggregation and sintering of metal particles under harsh conditions encountered in catalytic applications, e.g., in reactors or regenerators. Therefore, in the role of supports for metal NPs stabilisation, zeolites enhance the activity, selectivity, and lifespan of the metal catalysts.[17,18,19]

With their unique properties and cost-effective production, the application of zeolites ranges from detergents, adsorbents and ion-exchangers to highly efficient catalysts. Approximately, 10–12 different zeolites have been commercialised and are used as catalysts in industrial processes. Zeolites as heterogeneous catalysts represent a key and highly important class of catalysts employed in oil-refining and petrochemical industries with up to 40 % of the gasoline produced from the crude oil *via* fluid catalytic cracking (FCC). Other chemical processes where zeolites are utilised as catalysts include hydroxylation, alkylation, oximation, epoxidation, etc.[20,21]

In addition to traditional applications within chemical industries, these materials are gaining prominent recognition in sustainable chemistry and play a pivotal role in the fields of renewable energy and environmental enhancement, such as biomass conversion, fuel cells, thermal energy storage, CO_2 capture and conversion, water and air purification.[20,21]

2.2 Zeolites of MFI topology

Among the most studied zeolite topologies, the MFI topology stands out due to its eminent structural properties and significance in petroleum refining, petrochemicals and pollution control. Its origin arises from the successful synthesis of a material called ZSM-5 (Zeolite Socony **M**obil No. **Fi**ve) thanks to the work of scientists Argauer and Landolt.[22] ZSM-5 framework was afterwards assigned a three-letter code MFI.[10]

MFI topology is based on a pentasil structural unit (8 5-rings) linked to pentasil chains that represent the basis of the MFI framework (Figure 2). Ultimately, the MFI framework with corrugated MFI layers made of pentasil chains, and with present 10 T-atom pores results in the formation of a three-dimensional porous network (the system of straight channels along [010] axis and sinusoidal channels along [100] axis).[3,22]

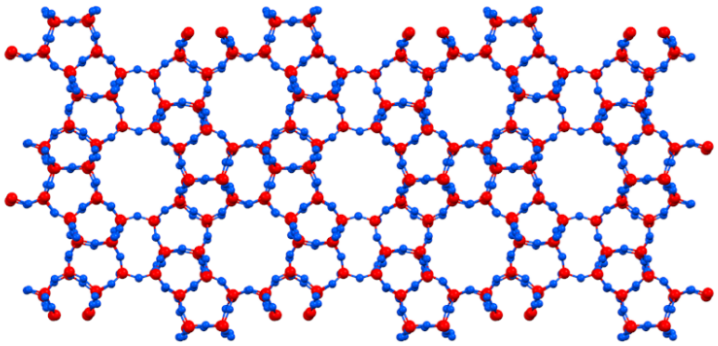

Figure 2. MFI framework structure with Si atoms in red colour and O atoms in blue colour. Generated from .cif file adapted from ref[10]

ZSM-5 material with a MFI topology can be synthesised with different architectures, ranging from 3D bulk zeolites, hierarchical architectures consisting of both micropores and mesopores to lamellar or nanosponge architectures of MFI (Figure 3).[23,24] MFI nanosponge zeolite architecture comprises an interconnected, disordered network of MFI nanolayers that are self-connected through crystalline pillars.[25,26] The thickness of nanosheets can be tailored by changing the properties of the SDA (e.g., a number of ammonium groups) restraining the propagation in the third direction with the possibility of obtaining a thickness of 1.5–3 nm. A typical example of the SDA used for the preparation of MFI nanosponge architecture is $C_{22}H_{45}–N^{+}(CH_3)_2–C_6H_{12}–N^{+}(CH_3)_2–C_6H_{13}$ denoted as $C_{22\text{-}6\text{-}6}$.[25] Mesopores between neighbouring nanosheets introduce extra surface area accessible for bulky molecules. This opens new possibilities for the application of such material in catalysis.[26,27]

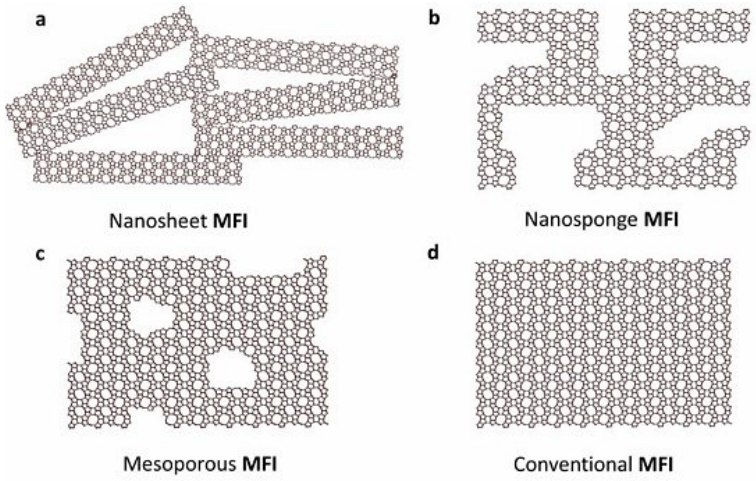

Figure 3. Schematic illustration of MFI zeolite architectures: (a) nanosheet, (b) nanosponge, (c) mesoporous, and (d) conventional bulk, excerpted from ref[24]

2.3 Zeolite-supported metal nanoparticles

Metal nanoparticles anchored to zeolites represent an important type of materials widely applied in many catalytic processes, such as CO/CO_2 hydrogenation and selective catalytic reduction of NO_x.[28] These catalysts possess favourable properties, such as a low mass-to-surface ratio caused by the small size of incorporated metal species. The size of particles anchored to zeolites is a vital parameter in their eventual catalytic performance. According to their size, metal particles are classified as bulk particles (>100 nm), nanoparticles (1–100 nm), sub-nanometric species and clusters (<1 nm), and finally even as isolated atoms in the case of single atom catalysts (SAC).[29,30,31] However, these catalysts suffer from deactivation under harsh conditions, e.g., high temperatures, due to the sintering of metal species.[31]

Zeolites with ordered microporous systems and their intrapore spatial nanoconfinement effect can provide a tailorable control of metal particles location, distribution and coordination environment. Therefore, metals incorporated onto zeolites can combine both the merits of metal active sites for catalysis and the intrinsic properties of zeolites as supports to stabilise the metal nanoparticles and inhibit their leaching and sintering.[32]

Furthermore, the introduction of the secondary metal in combination with the main primary metal has been shown as a promising way how to enhance the properties of the heterogeneous catalyst, such as catalytic activity, selectivity, dispersion and size distribution of metal species with improved stability. For example, such behaviour was observed in the case of nano P zeolite modified with Au/Cu bimetallic nanoparticles for hydrogen evolution reaction in contrast to monometallic counterparts.[33] This favourable catalyst enhancement encourages wide employment of bimetallic catalysts in the industry, e.g., in the process of hydroisomerisation of light parafines.[34,35]

Metal nanoparticles are commonly introduced to zeolites either by post-synthesis modifications (such as wet impregnation, ion-exchange, and template-guidance approach) or by in-situ encapsulation during the hydrothermal synthesis. Currently, an emerging approach for depositing metal nanoparticles arises, employing mechanochemical impregnation, applicable under both wet and dry (solvent-free) conditions.[36,37]

2.4 Mechanochemistry

Scientist W. Nernst classified and divided the fields of chemistry according to the type of energy used to activate the processes into thermochemistry, electrochemistry and photochemistry.[38] In recent years, a novel field of chemistry where mechanical energy is supplied to the system gained momentum, driven by its promising revolutionary future impact on the industrial synthesis. This field was designated as mechanochemistry.[39] There are plenty of processes that occur simultaneously while solids are being ground, namely reduction in particle size, generation of large new surfaces, formation of defects, phase transformation of materials and even activation of chemical reactions.[38]

In mechanochemical applications, a ball mill is commonly employed as a grinding tool. Grinding balls or other grinding media are used to reduce the size of various materials inside grinding jars. The configuration of the machine's parameters is a key factor for an optimal operation. The main ball mill parameters are frequency (Hz/rpm), and time duration. Moreover, the milling condition can be also adjusted by changing the material and volume of the grinding jars, and simultaneously by varying material, diameter and number of rigid balls used as grinding media. Nevertheless, ball milling can help automatise and scale-up catalyst synthesis processes while preserving a high level of synthesis efficiency.

2.4.1 Mechanochemistry and zeolites

Mechanochemistry has gradually emerged as a potentially useful methodology in zeolite science.[6] There are many possible applications of mechanical force on zeolites during their pre-treatment, synthesis, or post-treatment. One of the main advantages of the mechanochemical approach are solvent-free (SF) conditions that limit the production of wastewater and waste organic solvents. This green trait of the mentioned technique is noticeable during the activation of raw materials prior to the zeolite crystallization, milling of seed crystals for a zeolite synthesis and later post-synthetic modification of textural properties of prepared zeolites.[6]

Another key advantage of mechanochemistry are its adjustable parameters that allow the milling conditions to be precisely tailored for specific purposes. For low energy applications with configurated lower frequencies, zeolites interact with surrounding reactive species (such as metal precursors for metal NPs) in processes of wet

impregnation, ion-exchange and catalytic reactions.[5] In medium energy applications, modification of framework bonds and activation of material occurs. For example, a successful mechanochemical solid-state ion-exchange introduction of Sn^{4+} into a dealuminated Beta zeolites provided highly Lewis acidic Sn-Beta zeolite.[40] High-energy applications can lead to total amorphisation or recrystallisation of the zeolite as it was observed in the case of zeolite A with a kalsilite and a kaliphilite formed as recrystallisation byproducts.[40]

2.5 Lignin

Lignin represents the most abundant reservoir of renewable carbon and a resource of aromatic compounds. Around 3×10^{11} metric tons of lignin have been estimated to be found on the Earth, increasing annually by 2×10^{10} metric tons, while 5×10^{7} metric tons are yearly extracted by the industry.[41,42] Lignin, together with cellulose and hemicellulose, composes lignocellulose, a major building material of hardwoods, softwoods and herbaceous plants (Figure 4). So far, its low-value applications as high calorific value-energy source/fuel are insufficient to be profitable for biorefineries. Nevertheless, its high potential in the production of value-added chemicals cannot be neglected. However, its utilisation and valorisation are hindered by its complex heterogeneous, polymeric nature, strong odour, and high bond-dissociation energies of functional groups and bond linkages present in lignin.[2] An eminent effort has been invested into improving the efficiency of lignin depolymerisation, and further valorisation and upgrading processes to produce fine chemicals.[2,8,43,44,45]

The chemical structure of lignin varies significantly based on the taxonomy of the plant lignin comes from. Moreover, its chemical structure is modified upon isolation process, and it is highly dependent on the applied isolation methodology. The biopolymer consists of 3 main phenylpropane units – hydroxycinnamyl alcohols: guaiacyl propanol (also known as coniferyl alcohol – G unit), syringil propanol (synapil alcohol – S unit) and *p*-hydroxyphenyl propanol (*p*-coumaryl alcohol – H unit). These three compounds differ in their degree of methoxylation (Figure 4). Lignin coming from softwood is predominantly composed of G units, in hardwood G, S and H units can be found while in herbaceous plants G units prevail with a small amount of H units.[2,43,44] The diversity of types of bonds between phenylpropane units present in lignin is the reason for its structural complexity. Phenylpropane units are connected to the biopolymeric network

by C–O (ether linkages: α–O–4, β–O–4, 4–O–5, etc.) bonds, and C–C (condensed linkages: β–1, 5–5, β–5, etc.) bonds. The exact ratios of linkages in lignin depend on different ratios of phenylpropane building units present in a particular lignin sample.[2,8,43,44,45]

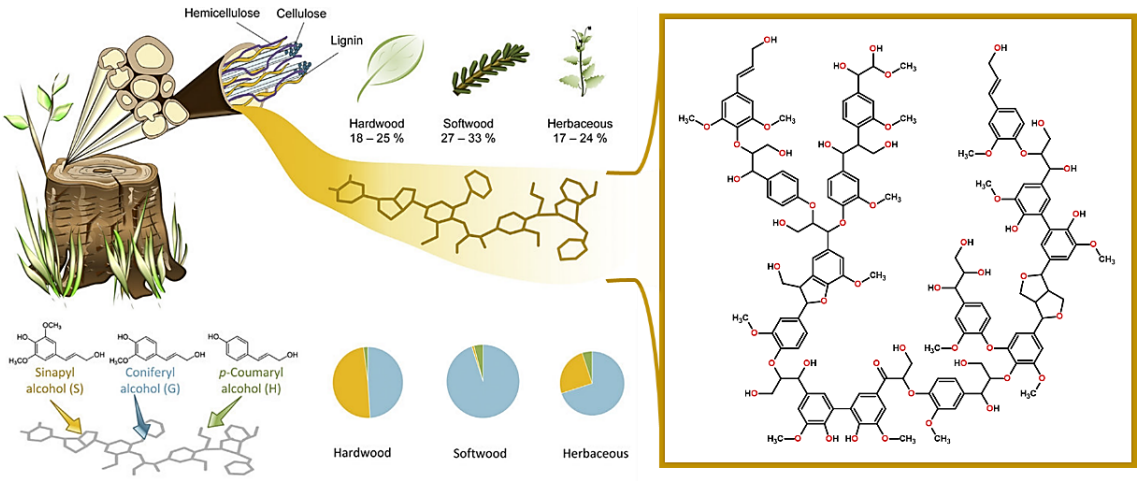

Figure 4. Lignin origin and occurrence in various plant taxonomies alongside the representation of its complex structure with 3 main structural phenylpropane units presented. Adapted from ref[46]

2.6 Hydrogenation of eugenol

Eugenol ($C_{10}H_{12}O_2$) is a phenolic organic compound found in cloves, their oils and essences. It is a pale-yellow oily liquid of characteristic spicy penetrating aroma with intrinsic antibacterial, antifungal, anticancer and antioxidant properties. Eugenol is widely used in the fields of medicine, cosmetology and pharmacology due to the rising emphasis on the use of traditional medicines with natural ingredients as active substances.[47]

Eugenol belongs to the group of model molecules for lignin valorisation since its chemical structure possesses functional groups such as phenyl, hydroxyl, methoxy and allyl groups that are also directly or indirectly present in all three of the main building components of lignin – phenylpropane units. Processes such as catalytic hydrogenation, hydrodeoxygenation and isomerisation represent three main ways of upgrading bio-oils to produce value-added chemicals from lignin. Such reactions are performed at moderate temperatures (200–450 °C) and elevated pressures (2–30 MPa). However, hydrodeoxygenation and aromatic hydrogenation under milder temperatures (<200 °C) are known to proceed with difficulties.[8,48]

In the hydrogenation of eugenol, different products can be formed *via* various pathways depending on the reaction conditions and the type of the catalyst used (Figure 5). The hydrogenation of a terminal double bond on the allylic group leads to the formation of 2-methoxy-4-propylphenol as the main product. Moreover, the formation of additional minor products, such as isoeugenol with its terminal double bond shifted to the neighbouring carbon atom, and other hydrogenated and hydrodeoxygenated products is observed (Figure 5). Hydrogenation and hydrodeoxygenation of aromatics progress under suitable reaction conditions and are dependent on the catalysts.

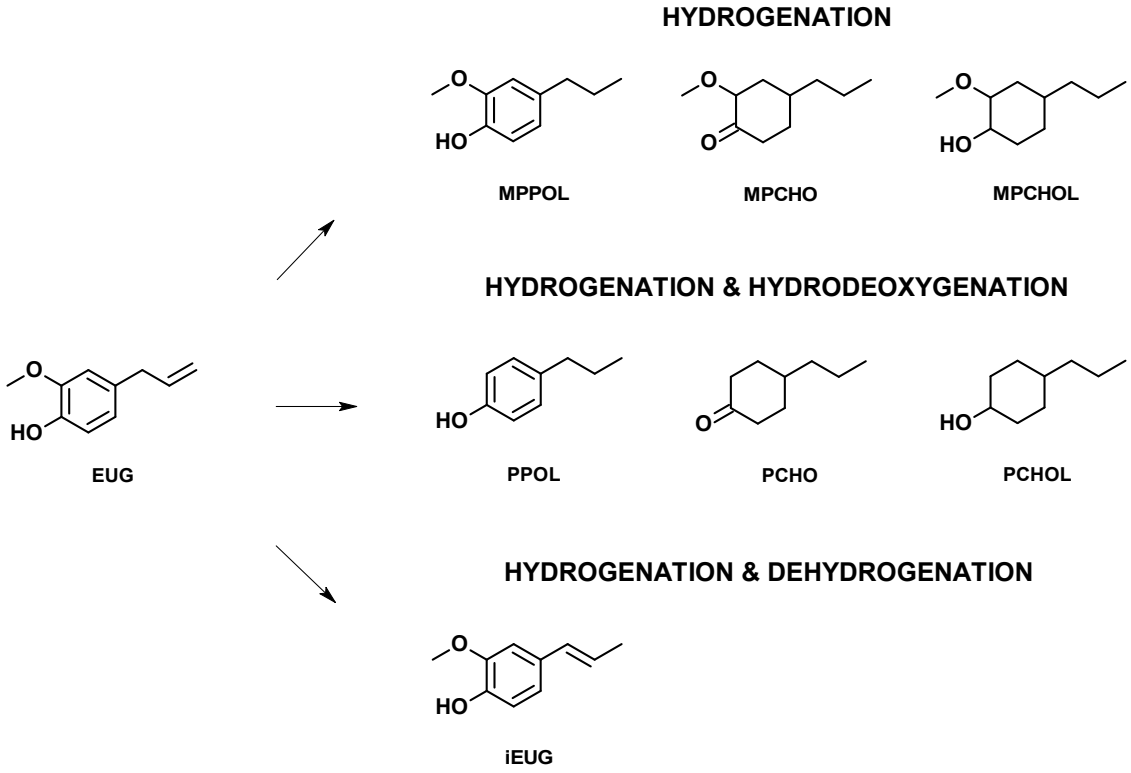

Figure 5. Observed catalytic hydrogenation, hydrodeoxygenation and hydrogenation-dehydrogenation products of eugenol transformation[8,45,48]

2.7 Characterisation methods

2.7.1 Powder X-ray diffraction (PXRD)

X-ray diffraction is a common non-destructive technique applied for the study of crystalline materials. It provides information on the structure of the material, its phases, preferred crystal orientation, average crystallite size, etc. This technique is based on the constructive interference of monochromatic X-rays and the analysed crystalline material. The phenomenon of diffraction can be observed only when the wavelength of incident waves is of the same order as the repetitive distance between scattering objects.

Copper is the most common target material used in anodes for emitting X-rays of the characteristic wavelength in the range of interatomic distances – λ (Cu Kα) = 1.5418 Å. X-ray radiation elastically scatters from electron density periodically distributed in a crystal lattice with the same frequency and wavelength as an incident wave. The relation among diffraction angle, wavelength and interplanar spacing of crystalline material is described by Bragg's law (Equation 1, Figure 6) with variables n representing an integer, λ stands for the wavelength of X-rays, d meaning the interplanar spacing and θ representing a diffraction angle:[49,50]

$$n\lambda = 2d \sin\theta \quad (1)$$

Single crystal X-ray diffraction is also a profound and powerful technique useful in structure determination of zeolites whereas powder X-ray diffraction serves mainly for rapid and easy identification and purity check of powder zeolite samples.[51]

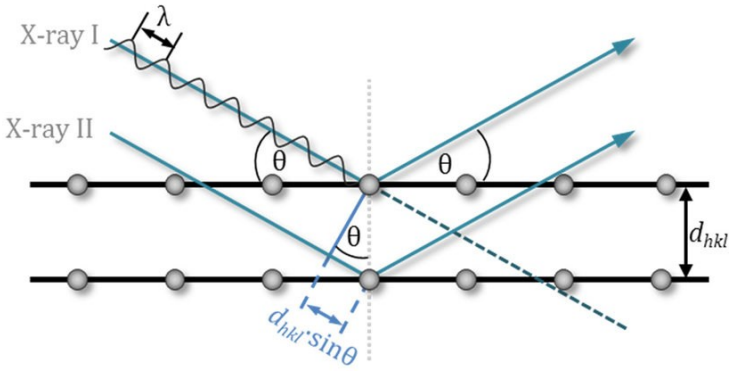

Figure 6. Graphical representation of Bragg's law[52]

2.7.2 Nitrogen sorption

Gas adsorption is a well-established technique in the characterisation of porous materials and their textural properties. Two subclasses of gas adsorption are distinguished: chemisorption and physisorption. The latter one, physisorption, refers to the phenomenon when an adsorbable gas (adsorptive) comes in contact and interacts with the surface of a solid (adsorbent) due to van der Waals forces, London dispersion forces and other interactions. The phenomenon is governed by the interplay of the strength of interactions between adsorptive–adsorbent and adsorptive–adsorptive interactions simultaneously with the state and thermodynamic stability of adsorptive confined to narrow pores of porous materials. All these aspects are reflected in the shape and type of adsorption isotherm which represents a relation between the adsorbed amount and the equilibrium pressure of an adsorptive at constant temperature. A classification of isotherms (Figure 7) and hysteresis loops (Figure 8) has been

published by the International Union on Pure and Applied Chemistry (IUPAC). Typically, as an adsorptive, liquid argon and liquid nitrogen are used at their boiling temperatures of −185.8 °C and −195.8 °C respectively.[53,54]

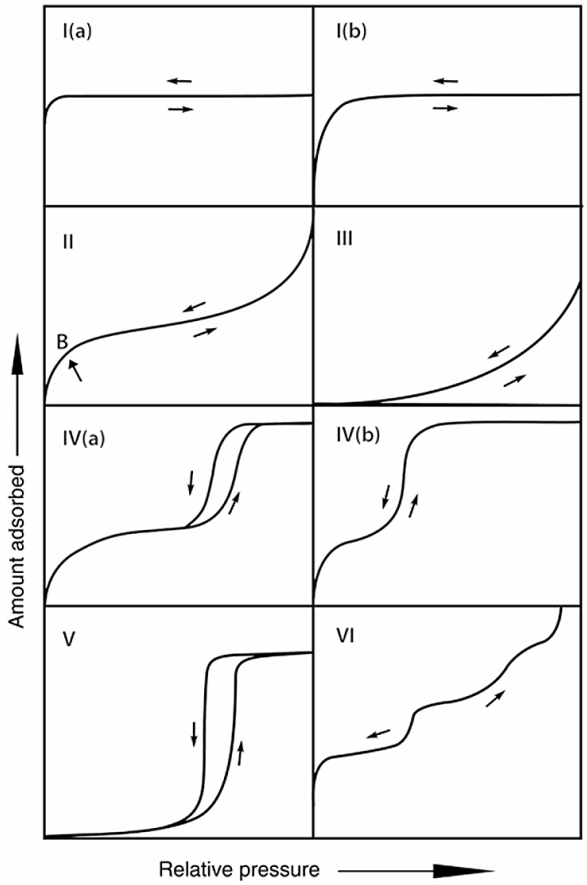

Figure 7. Classification of physisorption isotherms[55]

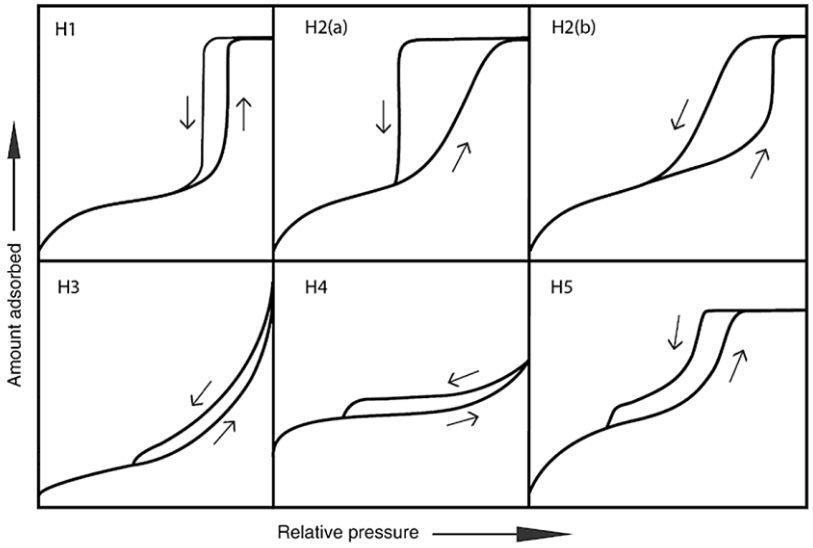

Figure 8. Classification of hysteresis loops[55]

The analysis of textural properties using physisorption is vital in the field of catalyst design and heterogeneous catalysis. The surface area of the catalyst can be estimated using Langmuir theory, assuming the monolayer gas adsorption. The volume of the adsorptive necessary to form a monolayer allows the calculation of the surface area. Brunauer-Emmet-Teller (BET) method, an extension of the Langmuir theory which introduces multilayer adsorption, approximately determines the accessibility of active sites essential in catalytic activity. BET method is commonly applied for practical measurements. For its evaluation, firstly, BET monolayer capacity n_m is derived from the linearised form of physisorption isotherm (Equation 2) presented below where p represents the pressure, p^0 saturation pressure, n represents the adsorbed amount, while n_m the mentioned monolayer capacity, and lastly, C representing BET constant:[54,55]

$$\frac{\frac{p}{p^0}}{n\left(1-\frac{p}{p^0}\right)} = \frac{1}{n_m C} + \frac{C-1}{n_m C} \times \frac{p}{p^0} \tag{2}$$

This monolayer capacity is defined as the amount of adsorptive sufficient to cover the surface with a complete monolayer. Next, the total surface area S_{total} (Equation 3) and the specific surface area S_{spec} (Equation 4) are calculated provided the value of the molecular cross-sectional area σ_m accordingly with N_A representing the Avogadro constant and m mass of the adsorbent:[54,55]

$$S_{\text{total}} = \sigma_m \, N_A \, n_m \tag{3}$$

$$S_{\text{spec}} = \frac{S_{\text{total}}}{m} \tag{4}$$

The pore architecture controls transport phenomena and governs shape selectivity in catalysis, particularly properties such as the pore volume, e.g., the volume of micropores V_{micro}, mesopores V_{meso}, the total pore volume V_{total}, and additionally the pore-size distribution. To perform a pore size analysis of zeolites we come across plenty of challenges. The filling of micropores with diameters of dimensions 0.1–1 nm arises at relative pressures in the range between 10^{-7} to 10^{-5}. The rates of diffusion of an adsorptive at equilibrium are very low and adsorption in the pores can amount to 7 orders of magnitude in the pressure values. Argon as an adsorptive turns out to be the best gas adsorptive due to the observed weaker fluid-pore wall attractions for most adsorbents in contrast to the gases such as nitrogen or carbon dioxide. In addition, argon does not specifically interact with an array of surface functional groups during the adsorption.[54] The optimisation of all these parameters is a target of a catalyst design.[53,56]

2.7.3 Electron microscopy

2.7.3.1 Transmission electron microscopy (TEM)

Microscopy has long been employed as a fundamental technique for material analysis, allowing the visualisation of structures beyond the limitations of human vision and improving the resolution. Scientist E. K. Abbe declared at the end of the 19th century that the optical microscope resolution is limited by the wavelength of visible light. In the early 20th century, physicists led by L. de Broglie discovered the wavelike character of electrons.[57] Scientists E. Ruska and M. Knoll improved the resolution of microscopes using accelerated electrons. Their successful construction of the first magnetic lenses led eventually to the development of the first transmission electron microscope (TEM) in 1931. The implementation of spherical aberration-corrected lenses to TEM in the late 1990s introduced new horizons in electron microscopy achieving sub-angstrom resolution and improving signal-to-noise ratio.[58,59,60]

The function of a TEM microscope (Figure 9) resembles the function of optical microscopes. The principle differs by using accelerated high-energy electrons (typically 30–300 keV; with specialised instruments reaching even 2000 keV)[61,62] to interact with the material. Electrons are emitted from the electron gun and then accelerated. There are 3 main types of electron guns used in an electron microscope: thermionic emission electron gun, field emission electron gun, and Schottky type emission electron gun.[57] The paths of electrons are subsequently shaped and focused to form a small uniform electron beam by condenser lenses. Excessive electrons are excluded from the beam by a condenser aperture. Direct electrons interact with a thin layer of sample, some passing through the sample (transmitted electrons) while others are scattered. Transmitted electrons are subsequently focused by objective lenses to form an image which is magnified by intermediate and projector lenses onto a phosphorescent screen or various types of electron cameras.[59]

The application of TEM in zeolite science covers various aspects of zeolite characterisation. It is crucial in determining the structures of new zeolites employing different modes of electron microscopy, such as high-resolution transmission electron microscopy and electron diffraction. Furthermore, TEM in combination with electron diffraction excels in the structural analysis of individual nano- or submicron-sized

crystals while methods such as X-ray diffraction provide details about the entire analysed sample.[63]

2.7.3.2 Scanning transmission electron microscopy (STEM)

STEM is a very powerful and versatile technique with the capability of obtaining atomic resolution images and nanoscale analysis of the specimen. In a TEM microscope in a scanning mode, electrons (energies of 100–300 keV) are focused into a beam of spot-like diameter and used for scanning across a sample surface. Signals from transmitted electrons are recorded by a set of various detectors positioned below the specimen. The annular dark-field (ADF) detector collects transmitted electrons scattered at high angles (>>10 mrad)[58] while the annular bright-field (ABF) detector collects electrons at low scattering angles (<10 mrad). STEM instruments of aberration--corrected systems of objective lenses and special monochromators can provide a resolution of even below 0.5 Å.[64] Alongside the STEM imaging of samples, additional spectroscopic methods such as EDS and EELS can be performed allowing high spatial resolution in elemental mapping of the specimen.[63,65,66]

In the analysis of zeolites, a key limiting factor in their STEM imaging at atomic resolution is the damage to the zeolite framework caused by an electron beam. This phenomenon occurs due to the high-intensity electron probe destroying the structure of zeolites and promoting their amorphisation.[63]

STEM plays a key role in the study of the zeolite structure and the pore system. Furthermore, it is used to analyse metal species stabilised at zeolites. For the zeolite-supported metal nanoparticles, Z-contrast plays a pivotal role in a direct visualisation of metal species anchored to a zeolite. This term refers to the contrast observed in high-angle annular dark-field STEM (HAADF-STEM) images that arises due to atomic number (Z) differences among elements of composition. The heavy metal nanoparticles appear brighter (Au, Pt, Pd, …), while the lighter support remains dim.[67]

2.7.3.3 Scanning electron microscopy (SEM)

SEM is used for analysis of larger (fractions of μm to several cm) specimens relative to TEM to give details about their structure topography, morphology, and chemical composition. For the image formation, primary electrons of an electron beam (electrons energies of 1–30 keV) are focused into a small-diameter probe that scans the surface of a sample. With a SEM microscope (Figure 9), resolutions in the range from 1 μm to

1 nm can be achieved with images of large depth of focus. Obtained information for the image formation comes from various interactions between the beam and the specimen leading to the collection of detected signals. Secondary electrons (SE) are electrons dislodged from shallow near-surface levels of the specimen atoms and are responsible for the topographic information. Backscattered electrons (BSE) are incident electrons travelling very closely to the nuclei of specimen atoms, and they are eventually scattered through a large range of angles. Mostly, they provide the compositional information.[68,69]

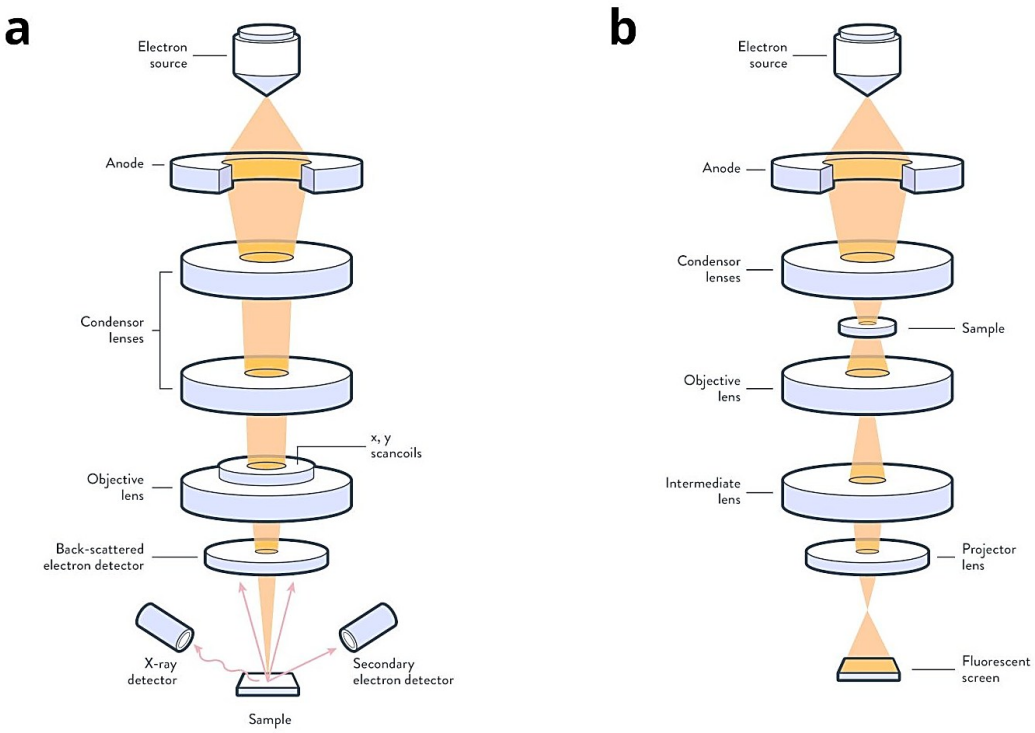

Figure 9. Schematic illustration of (a) SEM microscope and (b) TEM microscope adapted from ref[70]

2.7.3.4 Energy-Dispersive X-ray spectroscopy (EDS)

Energy-Dispersive X-ray spectroscopy is a rapid and frequent technique for the chemical characterisation of materials and their imaging with the possibility of obtaining elemental maps. High spatial resolution and high-count rates within a short time can be achieved in a TEM, STEM and SEM microscope. It works on a principle that primary incident electrons dislodge inner shell electrons of sample atoms *via* excitation creating a hole that is immediately refilled while an energy in the form of X-rays or Auger electrons is radiated. The released energy is characteristic for each core electron energy level allowing performing the compositional analysis.[65,71]

2.7.4 Temperature-programmed reduction (TPR)

TPR represents a technique applied for characterisation of metal and metal oxide catalysts. Typically, during a TPR experiment, a known mass of the catalyst is placed in a fixed-bed reactor and exposed to the flow of a reducing gaseous mixture (e.g., H_2) while linearly increasing the temperature. Outlet gas concentration is measured over time, commonly using a thermal conductivity detector, and subtracted from the constant inlet gas concentration to determine the amount of gas interacting with the sample. The final TPR profile obtained offers qualitative insights into the oxidation states of the reducible metal oxide species and identifies temperatures required for their reduction.[72]

2.7.5 Gas chromatography

Gas chromatography is an analytical method that utilises a capillary column under controlled temperature programmed conditions to separate individual components of a gasified analysed mixture into individual components and subsequently measure the amounts of each component using a suitable detector (Figure 10). This method is typically applied to the analysis of the mixtures with components of boiling points up to 450 °C (in the case of HT-GC up to 800 °C), and with low susceptibility towards thermal decomposition.[73,74]

Separations are achieved *via* continuous partitions occurring between a carrier gas phase and a stationary active phase sited in the column placed in the oven following the injection of the sample mixture. The unreactive carrier gas (nitrogen, helium, hydrogen, argon, etc.) as a mobile phase enables to transfer a sample through the column. The mentioned partitions arise based on varying chemical and physical properties (such as boiling temperatures) of the mixture components and simultaneously based on their interaction with a stationary phase of the column. Separated compounds present in the gas stream are then eluted from the column at different times – retention times and monitored by the detector. Detectors used are of various types, e.g., FID – flame ionisation detector, FPD – flame photometric detector, and TCD – thermal conductivity detector. Implementation of MS – mass spectrometry detectors enables the acquirement of structural information and specificity of the compounds during the analysis of complex mixtures. Obtained signals provide the final input for successive data evaluation.[73]

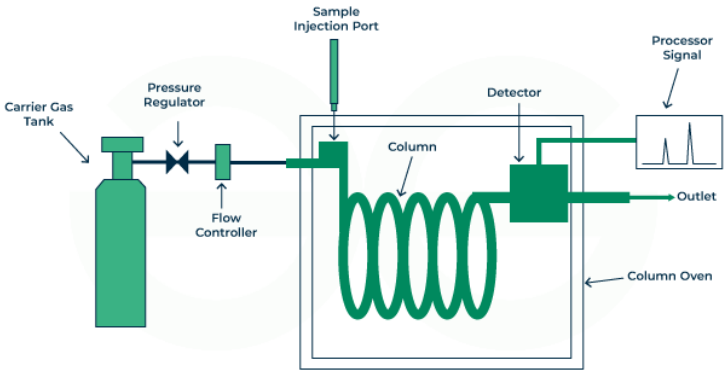

Figure 10. Schematic diagram of gas chromatography system adapted from ref[75]

Resulting signals are represented in the form of chromatographic peaks visible in the chromatogram. Areas of peaks corresponding to the detected individual compounds strictly correlate to their molar amounts in the injected mixture. Furthermore, to monitor changes of molar amounts and thus concentrations of compounds of the reaction mixture in time, an internal standard – inert molecule with an unchanged molar amount for the duration of the followed reaction, can be added to the mixture and thus serves as a reference compound.

3 Experimental part

3.1 List of chemicals

Table 1. List of chemicals used for the zeolite synthesis, its impregnation and catalytic experiments

Chemical	Purity	Manufacturer
1-Bromohexane	98%	Sigma Aldrich
1-Bromooctadecane	97%	Alfa Aesar
1-Hexanol	99%	Alfa Aesar
2-Propanol	≥98%	VWR Chemicals
Acetonitrile	≥99%	Sigma Aldrich
CAB-O-SIL M5	-	Acros Organic
Cerium(III) nitrate hexahydrate	99.99%	Sigma Aldrich
Copper(II) nitrate hemipentahydrate	98%	VWR Chemicals
Diethyl ether	100%	VWR Chemicals
Ethyl acetate	-	VWR Chemicals
Ethylenediamine	≥99.5%	Sigma Aldrich
Eugenol	99%	Thermo Scientific
Gallium(III) nitrate hydrate	99.9%	Sigma Aldrich
Hydrochloric acid	37%	VWR Chemicals
Lanthanum(III) nitrate hexahydrate	99.99%	Sigma Aldrich
N,N,N',N'-tetramethyl-1.6-diaminohexane	≥98%	TCI Chemicals
n-Dodecane	≥99%	Sigma Aldrich
Nickel(II) nitrate hexahydrate	≥98.5%	Fluka
Nitric acid	65%	LACHNER
Rhodium(II) acetate dimer	99.9%	Sigma Aldrich
Ruthenium(III) chloride hydrate	99.98%	Sigma Aldrich
Sodium hydroxide	P.A.	LACHNER
Sulfuric acid	96%, P.A.	LACHNER
Tetraamminepalladium(II) nitrate, 10% in H_2O	99.99%	Sigma Aldrich
Tetraammineplatinum(II) nitrate	Pt (49.9–50.7%)	Thermo Scientific
Toluene	P.A.	LACHNER
Yttrium(III) nitrate hexahydrate	99.8%	Sigma Aldrich

3.2 Synthesis of structure directing agent (SDA)

The synthesis procedure of a structure directing agent was adapted from the procedure by Jo *et al*.[27] For the synthesis of SDA – $C_{18\text{-}6\text{-}6}$ [$C_{18}H_{37}$–$N^{+}(CH_3)_2$–C_6H_{12}–$N^{+}(CH_3)_2$–C_6H_{13}][Br^{-}]$_2$, firstly the mass of 16 g of 1-bromooctadecane and 81 g of N,N,N',N'-tetramethyl-1,6-diaminohexane were dissolved in the solvents mixture of 230 ml of toluene and 255 ml of acetonitrile. The reaction mixture was heated under the reflux at 60 °C overnight. The next day, the solvent was evaporated by a rotary evaporator, 200 ml of diethyl ether was then added to the product, and it was stirred for 3 hours. The flask with the SDA intermediate product was placed in the refrigerator overnight to finalise the precipitation. The next day, the product was filtered, washed with cooled diethyl ether, and dried overnight in the hood.

In the second step of the SDA synthesis, 25 g of prepared intermediate product was dissolved with 8.16 g of 1-bromohexane in the solvent mixture comprising 230 ml of toluene and 255 ml of acetonitrile. Heating, evaporating, cooling, filtration and drying were repeated in the same way as mentioned in the first step of the SDA synthesis procedure above.

3.3 Synthesis of degallated MFI nanosponge

Degallated MFI nanosponge was synthesised similarly to the procedure presented by Jo e*t al.*[27] Firstly, 3.75 g of NaOH was dissolved in 50 ml of distilled water. Then, the hydroxide solution was transferred to a plastic container and the mixture of 10 g of CAB-O-SIL M5 pre-dissolved in 30 ml of distilled water was added. The mixture in the closed plastic container was shaken by hand vigorously and stirred for 10 minutes using an agitator of a mechanical stirrer. After 10 minutes, 8.35 g of the SDA ($C_{18\text{-}6\text{-}6}$) was added to the mixture which was left to stir overnight. The next day, an aqueous solution of 0.85 g of gallium nitrate hydrate and 10 ml of distilled water was added dropwise to the stirred mixture. Subsequently, a solution of 1.64 ml of concentrated H_2SO_4 and 30 ml of distilled water was added dropwise to the mixture which was left to stir overnight. The next day, the mixture was split into two portions and transferred to two autoclaves. The autoclaves were placed into the tumbling oven for 192 hours at the temperature of 150 °C. After that, the prepared zeolite was washed using distilled water, filtered and dried at 60 °C overnight. The zeolite was calcined under air at 550 °C for 6 hours at a temperature rate of 1 °C/min.

Prepared gallosilicate was degallated using concentrated HNO_3. 9 g of prepared zeolite was mixed with the 900 ml of concentrated HNO_3 and heated under reflux at 100 °C overnight. Then, degallated zeolite was filtered from the mixture and washed with distilled water until the neutral pH was reached. Filtered degallated MFI nanosponge was then dried at 60 °C overnight and calcined under air at 550 °C for 6 hours with a temperature rate of 1 °C/min.

3.4 Impregnation of degallated MFI nanosponge

Mechanochemical wet impregnation was performed by the ball mill Retsch MM 400 Mixer Mill (Figure 11). As grinding media, ZrO_2 grinding balls were used with a diameter of 10 mm (referred to as a big ball) and 5 mm (referred to as a small ball). Ball milling was performed in PTFE grinding jars of a volume of approximately 10 ml.

Manual wet impregnation was performed using the mortar and the pestle (Figure 11).

Figure 11. Images of the ball mill Retsch MM 400 Mixer Mill alongside PTFE grinding jars of volume of 10 ml and ZrO_2 grinding balls of diameter of 5 mm. The right image shows the mortar and the pestle.

3.4.1 Optimisation of mechanochemical impregnation method

In total, 8 ball milling tests were conducted after which a set of specific conditions was selected to be later applied for a mechanochemical wet impregnation. Changing parameters were frequency, time duration, and number × diameter of grinding balls (Table 2). As a testing material to optimise milling conditions, commercial zeolite ZSM-5 (Si/Al = 140) in NH_4^+-form was selected to mimic the use of prepared degallated MFI nanosponge.

Table 2. Milling test parameters

	Frequency of milling [Hz]	Time [min]	Number × Diameter of grinding media [pcs × mm]
Test 1	15	5	1 × 10
Test 2	15	5	3 × 5
Test 3	15	10	1 × 10
Test 4	15	10	3 × 5
Test 5	30	5	1 × 10
Test 6	30	5	3 × 5
Test 7	30	10	1 × 10
Test 8	30	10	3 × 5

For the testing procedure, 0.26 g of the commercial zeolite was loaded into a grinding jar and 0.3 ml of distilled water was added. Then, 1 big ball or 3 small balls were added to the mixture according to the testing parameters, grinding jar was closed and attached to the ball mill. The frequency of milling and its time duration were set on the ball mill and the milling was started. After the milling, the zeolite was dried in the oven. For further mechanochemical wet impregnation applications, milling conditions with parameters same as in Test 8 (Table 2) were applied.

3.4.2 Manually and mechanochemically impregnated Pt@MFI

To compare the efficiency of both wet impregnation approaches, total of 0.5 wt.% of Pt was anchored onto a zeolite.

3.4.2.1 Manually impregnated zeolite

A solution of 1.0 mg $[Pt(NH_3)_4](NO_3)_2$ and 0.1 ml of distilled water was added dropwise to 0.1 g of prepared zeolite in the mortar. The mixture was ground for 1 hour manually with the pestle. The sample was subsequently dried at 60 °C overnight and calcined under air at 350 °C for 2 hours with a temperature rate of 1 °C/min.

3.4.2.2 Mechanochemically impregnated zeolite

PTFE grinding jar was loaded with 0.1 g of prepared zeolite, 3 small grinding balls and the solution of 1.0 mg of $[Pt(NH_3)_4](NO_3)_2$ and 0.1 ml of distilled water was added dropwise. The mixture was ground at 30 Hz frequency for 10 minutes. The sample was

then dried at 60 °C overnight and calcined under air at 350 °C for 2 hours with a temperature rate of 1 °C/min.

3.4.3 Mechanochemical impregnation method for preparation of catalysts

Degallated MFI nanosponge was impregnated with platinum group metals (PGM) and transition metals (TM) with or without simultaneously co-impregnated RE elements to prepare bimetallic and monometallic catalysts respectively. The zeolite was impregnated by adding an impregnating solution containing the equivalent of 1 wt.% of a primary metal (Pt, Pd, Rh, Ru, Ni, Cu), with or without an additional 1 wt.% of a RE element (La, Ce, Y) to the support.

Mechanochemical impregnation of metals – Pt, Pd, Cu, Ni, La, Ce, and Y was performed in a following way: 0.35 g of prepared zeolites was loaded into the grinding jar. Then, the solution of appropriate amounts of metal and RE element precursors dissolved in 0.35 ml of distilled water was added. However, for Rh-impregnated and Ru-impregnated samples, the preparation of the impregnating solutions differed.

In the case of Rh-impregnated samples, rhodium precursor $Rh_2(O_2CCH_3)_4$ was dissolved in the solution of 0.41 ml of ethylenediamine, and 0.875 ml of ethanol and the solution was stirred and heated in a closed vial at the temperature of 65 °C till colour change from dark pink to yellow-brown colour was observed. In this way, the impregnating solution was prepared.

In the case of Ru-impregnated samples, ruthenium precursor $RuCl_3 \cdot xH_2O$ showed lower susceptibility to dissolve in 0.35 ml of distilled water, hence the mixture of 1.20 ml of concentrated HCl and 0.25 ml of distilled water was used for dissolving of the appropriate amount of the metal source. The prepared solution was stirred for 6 hours with a magnetic stirrer in a closed vial at 65 °C to fully dissolve the metal precursor.

After adding the impregnating solution to the grinding jars loaded already with the zeolite and 3 small zirconia balls, the mixture was ground at 30 Hz frequency for 10 minutes in the ball mill. The mixture was then dried at 60 °C overnight and calcined under air at 350 °C for 2 hours at a set temperature rate of 1 °C/min.

In the case of Ru-impregnated samples, the mentioned calcination step was performed under a reductive H_2 atmosphere in a tubular oven with the flow of H_2 set to 50 ml/min

at 350 °C for 2 hours with a set temperature rate of 3 °C/min. During the cooling process, H_2 was replaced with N_2.

Metal and RE element precursors used for impregnation are listed below (Table 3).

Table 3. Metal and rare-earth metal precursors

Metal	Source	Purity
Pt	$[Pt(NH_3)_4](NO_3)_2$, *ca.* 50 wt.% of Pt	~99 wt.%
Pd	$[Pd(NH_3)_4](NO_3)_2$, 10% in H_2O	99.99 wt.%
Ru	$RuCl_3 \cdot x\ H_2O$	99.98 wt.%
Rh	$Rh_2(O_2CCH_3)_4$	99.9 wt.%
Ni	$Ni(NO_3)_2 \cdot 6\ H_2O$	98.5 wt.%
Cu	$Cu(NO_3)_2 \cdot 2.5\ H_2O$	98 wt.%
La	$La(NO_3)_3 \cdot 6\ H_2O$	99.99 wt.%
Ce	$Ce(NO_3)_3 \cdot 6\ H_2O$	99.99 wt.%
Y	$Y(NO_3)_3 \cdot 6\ H_2O$	99.8 wt.%

A series of 12 prepared catalysts is listed below, along with calculated appropriate amounts of used precursors as metal sources (Table 4).

Table 4. Calculated amounts of precursors used for impregnation

Catalyst	1st Metal	Source amount [mg]	2nd Metal	Source amount [mg]
Pt@MFI	Pt	7.0	-	-
Pt-La@MFI	Pt	7.0	La	10.9
Pt-Ce@MFI	Pt	7.0	Ce	10.8
Pt-Y@MFI	Pt	7.0	Y	15.1
Pd@MFI	Pd	98.2	-	-
Pd-La@MFI	Pd	98.2	La	10.9
Pd-Ce@MFI	Pd	98.2	Ce	10.8
Pd-Y@MFI	Pd	98.2	Y	15.1
Rh@MFI	Rh	7.5	-	-
Ru@MFI	Ru	9.0	-	-
Ni@MFI	Ni	17.3	-	-
Cu@MFI	Cu	12.8	-	-

3.5 Characterisation of prepared materials

3.5.1 Structural characterisation

Bruker AXS D8 Advance diffractometer was used for the confirmation and analysis of crystalline structures of prepared materials. X-rays of the characteristic wavelength (Cu Kα) of 1.54 Å were used for the irradiation of samples. The diffraction patterns in the range of 1–40° or 1–50° 2θ were obtained.

3.5.2 Textural properties

Micromeritics 3Flex Version 5.01 was used for the study of textural properties of prepared materials, including surface area and pore volume. The temperature of the analysis bath was set to −195.85 °C (77.3 K) with an equilibration interval set in the range of 5–10 s. The BET model approach was used for the calculation of the total surface area of samples with p/p^0 in the range of 0.01–0.1. T-plot method was used for the calculation of micropore volume, micropore area and external surface of prepared materials.

3.5.3 Crystal morphology

The analysis of morphological properties of prepared samples was conducted with the use of a scanning electron microscope Thermo Scientific Scios 2 DualBeam. Images acquired by secondary and back-scattered electrons detectors were collected with an accelerating voltage of 2 kV, a beam current of 13 pA and a working distance of 4 mm.

3.5.4 Zeolite structure and metal particle analysis

Transmission electron microscope JEOL JEM NEOARM-200F set in a scanning mode was used for the imaging and analysis of structural properties of zeolite and examining the metal particles size and spatial distribution anchored to the support. Images were acquired by annular dark-field (ADF) and annular bright-field (ABF) detectors with an accelerating voltage of 200 kV. EX-37001 energy dispersive X-ray analyser was simultaneously employed for an elemental mapping analysis of prepared materials. Data required for the particle size distribution were collected using ImageJ (Fiji)[76] software and subsequently processed by Origin (OriginPro, Version 2022. OriginLab Corporation, Northampton, MA, USA).

3.6 Hydrogenation of eugenol

Catalytic reactions were performed in 4 parallel high-pressure stainless-steel batch reactors (PID Micromeritics) of a volume of 50 ml with a magnetic stirring rod and a sampling probe (Figure 12). Pressure, temperature and stirring were controlled by software in a real time.

Prior to the catalytic hydrogenation reaction, catalysts were reduced in a tubular reduction oven at H_2-TPR determined temperature *T* (Table 5) for 2 hours with a heating rate of 3 °C/min, and with the flow of hydrogen and nitrogen gas both set to the 30 ml/min each.

TPR analysis was conducted similarly as described by Kurbanova *et al.* using an AMI-300 Lite (Altamira Instruments) chemisorption instrument.[77] In a typical TPR experiment, around 100 mg of the catalyst was placed in the quartz U-shaped tube equipped with a thermocouple. Initially, the catalyst was dried under an argon atmosphere at 240 °C for 2 h. After cooling to the room temperature, the catalyst was heated from 50 °C to 1000 °C at a heating rate of 10 °C/min under a flowing gas mixture of 5 % of H_2 in Ar. The temperature of 1000 °C was held for 20 min. The mentioned procedure was repeated again after the catalyst had cooled to the room temperature.

Table 5. Reduction temperatures of prepared catalysts determined by H_2-TPR

Catalyst	*T* [°C]
Pt(-RE)@MFI	700
Pd(-RE)@MFI	550
Rh@MFI	500
Ru@MFI	550
Ni@MFI	450
Cu@MFI	400

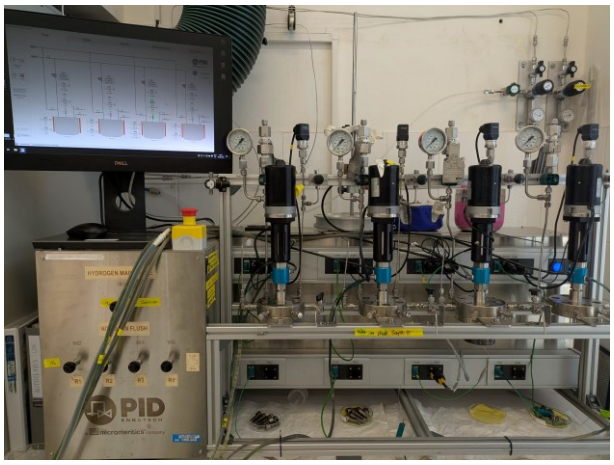

Figure 12. Four parallel high-pressure stainless-steel batch reactors with a controlling software

As for the reaction conditions in catalytic experiments, the pressure of hydrogen gas was set to 25 bars, the temperature to 150 °C and agitation to 1000 rpm.

In a typical catalytic hydrogenation experiment, batch reactors were loaded with 100 mg of a freshly reduced catalyst, 36 ml of the solvent 2-propanol, 0.7 ml of the internal standard *n*-dodecane and 1.6 ml of the reactant eugenol. The zero sample was collected at this point. After a leak check and the desired temperature of the reaction mixture (150 °C) was reached, the stirring speed was increased from 200 rpm to 1000 rpm and the hydrogen was introduced. The reaction lasted from this point for 6 hours while samples were collected *via* the sampling probe cooled by a cold dishtowel after 1, 2.5, and 4 hours. The last sample was collected after the opening of the reactor when the reaction mixture had cooled to the temperature of 63 °C.

For the analysis of collected samples, a gas chromatograph (GC) Agilent 8860 with an autosampler, HP-5 Agilent column (30 m × 320 µm × 0.25 µm), and an FID detector was used. The oven was set to 70 °C and the temperature was held for 2 minutes. Then, the temperature was increased to 250 °C with a heating rate of 10 °C/min. Signals from the GC in the form of peaks and their corresponding areas were multiplied by the response coefficients belonging to the compounds obtained upon the calibration.

The eugenol conversion x was calculated accordingly (Equation 5):

$$x = \frac{\frac{A_{e,0}}{A_{st,0}} - \frac{A_{e,t}}{A_{st,t}}}{\frac{A_{e,0}}{A_{st,0}}} \times 100\ \% \quad (5)$$

where $A_{e,0}$ stands for an initial area of the eugenol in the beginning, $A_{e,t}$ represents the area of the eugenol at a given time t, $A_{st,0}$ has the meaning of an initial area of the internal standard and $A_{st,t}$ represents the area of the internal standard at a given time t.

The yields of products y_i (i = iEUG, MPPOL, …) were calculated according to the formula below (Equation 6):

$$y_i = \frac{\frac{A_{i,t}}{A_{st,t}}}{\frac{A_{e,0}}{A_{st,0}}} \times 100\ \% \quad (6)$$

where $A_{i,t}$ represents the area of the product i at a given time t, and other variables stand for the same meaning as already mentioned above.

The selectivity towards each product s_i (i = iEUG, MPPOL, …) was calculated using Equation 5 and Equation 6 accordingly (Equation 7):

$$s_i = \frac{y_i}{x} \times 100\ \% \quad (7)$$

where y_i stands for the yield of the product i and x represents the eugenol conversion.

4 Results and discussion

A series of 12 catalysts was designed and prepared using the same zeolite as the support – degallated MFI nanosponge, containing various types of metal nanoparticles anchored to the support, with the loading of 1 wt.% of a primary metal and an additional 1 wt.% of a RE element if applied.

Initially, a zeolite – gallosilicate MFI nanosponge was hydrothermally synthesised followed by its post-synthesis degallation using concentrated nitric acid to generate silanol nests.[7] Consecutively, platinum group metals (PGM), i.e., Pt, Pd, Rh, Ru; and transition metals (TM), i.e., Ni, Cu; were mechanochemically impregnated onto the degallated zeolite as catalytically active metal species for the hydrogenation reaction. Rare-earth elements (La, Ce, Y) acted as metal promoters alongside a catalytically active primary metals (PGM, Pt and Pd specifically) in the case of bimetallic catalysts.

In total, 6 monometallic and 6 bimetallic materials were prepared. Samples were denoted according to the metals impregnated onto zeolite following the pattern X(-RE)@MFI, where X represented PGM or TM and (-RE) represented an optional presence of a RE element, e.g., Pt-Ce@MFI for degallated MFI nanosponge impregnated with Pt as a primary metal and Ce as a secondary metal. The catalytic performance of synthesised materials was studied in the eugenol hydrogenation reaction. Eugenol was selected as a model molecule for the process of lignin valorisation. This selection was due to its structural similarities to the lignin building units. Furthermore, eugenol can undergo both hydrogenation and hydrodeoxygenation reactions, yielding a diverse range of possible products[8], allowing full description of catalysts performance.

4.1 Optimisation of mechanochemical impregnation method

To implement ball milling in the process of wet impregnation, prior optimisation of the method was required. The goal was to preserve the structure of zeolite – MFI degallated nanosponge during milling while maintaining highly efficient impregnation of metal species. For this purpose, commercial zeolite ZSM-5 (Si/Al = 140) in NH_4^+-form was selected as a testing material. This available and relatively cheap material was used to mimic prepared degallated MFI nanosponge with same zeolite topology. Commercial zeolite samples were milled under 8 different conditions specified below (Table 6).

Table 6. Milling test parameters

	Frequency of milling [Hz]	Time [min]	Number × Diameter of grinding media [pcs × mm]
Test 1	15	5	1 × 10
Test 2	15	5	3 × 5
Test 3	15	10	1 × 10
Test 4	15	10	3 × 5
Test 5	30	5	1 × 10
Test 6	30	5	3 × 5
Test 7	30	10	1 × 10
Test 8	30	10	3 × 5

Structure preservation was monitored by investigation of XRD diffractograms of ground commercial zeolite samples in comparison to XRD diffractogram of its non-milled form (Figure 13, Figure 14).

In the Figure 13, a visible reduction in intensity of diffraction maxima and in their resolution indicated a degradation of the zeolite structure. This was attributed to the higher impact force of 1 (ø 10 mm) ZrO_2 grinding ball upon collisions. In the Figure 14, when 3 (ø 5 mm) ZrO_2 grinding balls were used for milling, intensities of maxima did not differ significantly and maintained their initial resolution. Moreover, no differences were observed in diffractograms of samples ball milled for 5 minutes compared to those milled for 10 minutes regardless of size and number of grinding balls used. Therefore, within the tested time range, this parameter did not show any recognisable effect on the support structure.

Test 8 indicated milling parameters allowing the preservation of the zeolite structure while maintaining high-frequency milling and effective impregnation. Hence, these conditions were selected for further mechanochemical wet impregnation of prepared degallated MFI nanosponge material (MFI-deGa-calc).

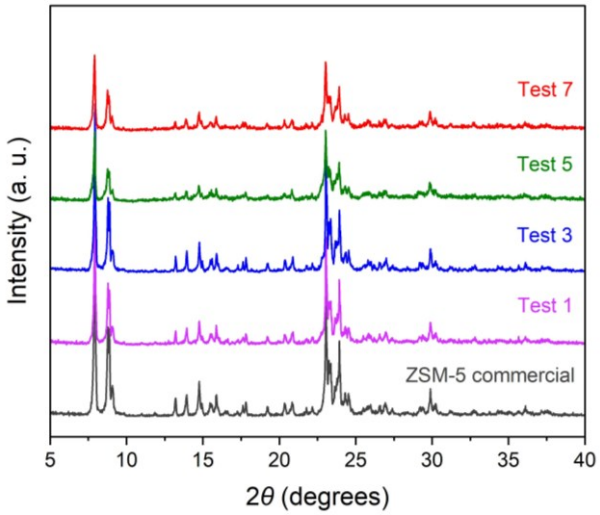

Figure 13. Investigation of structure preservation of commercial zeolite ZSM-5 (Si/Al = 140) in NH_4^+-form with PXRD diffractograms – milling with 1 (⌀ 10 mm) ZrO_2 grinding ball

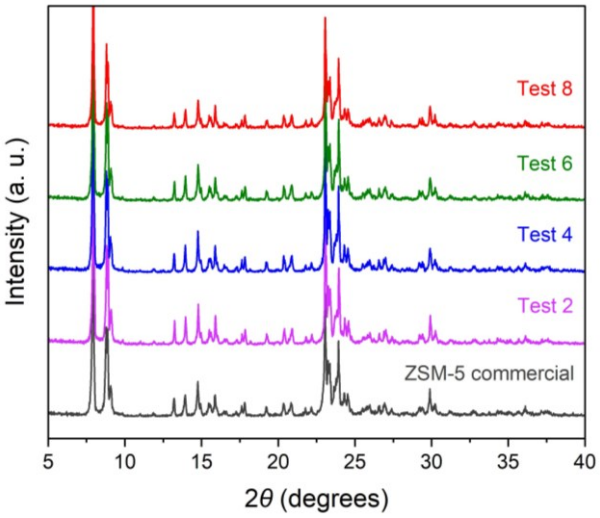

Figure 14. Investigation of structure preservation of commercial zeolite ZSM-5 (Si/Al = 140) in NH_4^+-form with PXRD diffractograms – milling with 3 (⌀ 5 mm) ZrO_2 grinding balls

4.2 Structure of prepared materials

Powder X-ray diffraction was used for the investigation of the structure of prepared materials. Calculated theoretical PXRD diffractogram of ZSM-5 zeolite corresponding to MFI zeolite topology was simulated from a .cif file from IZA database[10] and was compared to the diffractograms of as synthesised gallosilicate MFI nanosponge (MFI-gal-as), calcined gallosilicate MFI nanosponge (MFI-Ga-calc), as synthesised degallated MFI nanosponge (MFI-deGa-as) and calcined degallated MFI nanosponge (MFI-deGa-calc).

Positions and relative intensities of diffractogram peaks of MFI nanosponge materials correspond to the calculated theoretical positions of ZSM-5 of MFI zeolite topology indicating the synthesis of the structure of MFI topology. The PXRDs of obtained materials correspond also with the literature data for MFI nanosponge materials.[25] The preservation of zeolite structures after calcination and degallation was observed (Figure 15). Lower peak intensities and peak broadening were attributed to the preparation of the nanosponge type of a disordered defected structure with small zeolite crystallites formed.[27]

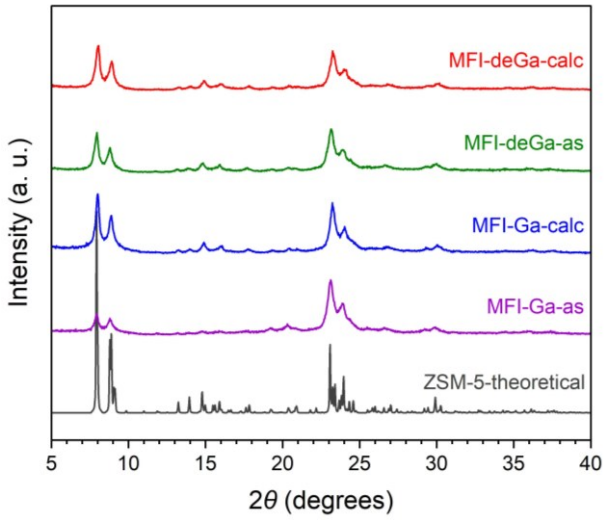

Figure 15. PXRD diffractograms of calculated theoretical ZSM-5 material[10] and prepared MFI nanosponge supports. Characteristic peak positions around 8°, 9°, 23° and 24° 2θ confirmed MFI nanosponge architecture of prepared materials

In addition, the comparison of PXRD diffractograms of manually and mechanochemically impregnated Pt@MFI nanosponge samples was performed (Figure 16). Observed highly similar diffractogram of the mechanochemically impregnated sample Pt@MFI-BM to the diffractogram of the manually impregnated sample Pt@MFI-MAN confirmed material structure preservation after milling. The structure preservation was accomplished based on the correct selection of milling parameters for mechanochemical impregnation during the optimisation process.

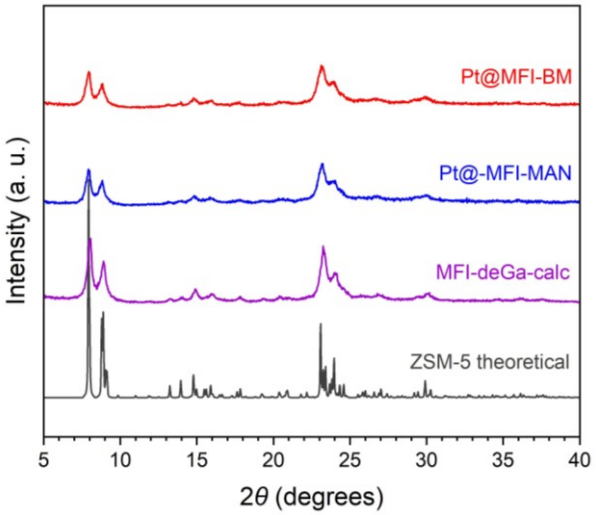

Figure 16. PXRD diffractograms of calculated theoretical ZSM-5 material[10], MFI-deGa-calc zeolite and prepared Pt@MFI materials *via* manual (Pt@MFI-MAN) and mechanochemical (Pt@MFI-BM) wet impregnation method

In a similar manner, all mono- and bimetallic nanoparticles doped degallated MFI nanosponge materials prepared by mechanochemical wet impregnation method exhibited highly similar diffractograms to MFI-deGa-calc sample confirming the preservation of MFI nanosponge architecture even after high-frequency ball milling impregnation (Figure 17–19). In addition, no diffractogram peaks corresponding to impregnated metals in the form of their oxides (typically positioned at 30–40° 2θ) were observed, indicating very small and well-dispersed metal species.

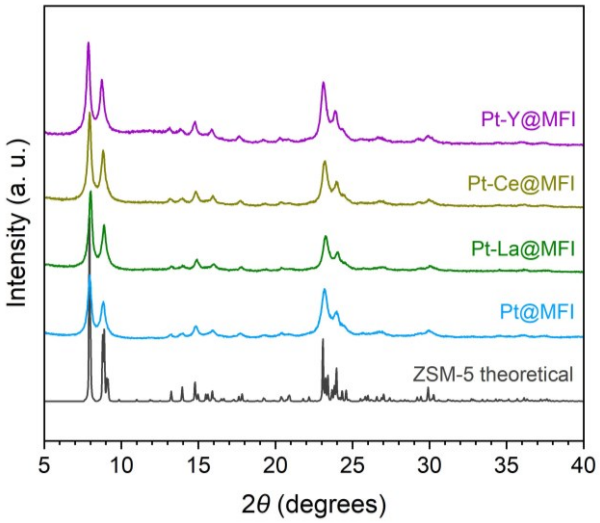

Figure 17. PXRD diffractograms of calculated theoretical ZSM-5 material[10], and prepared Pt(-RE)@MFI nanosponge materials

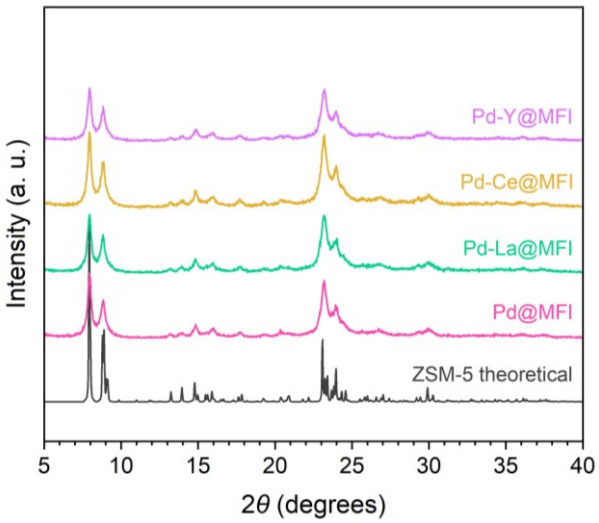

Figure 18. PXRD diffractograms of calculated theoretical ZSM-5 material[10], and prepared Pd(-RE)@MFI nanosponge materials

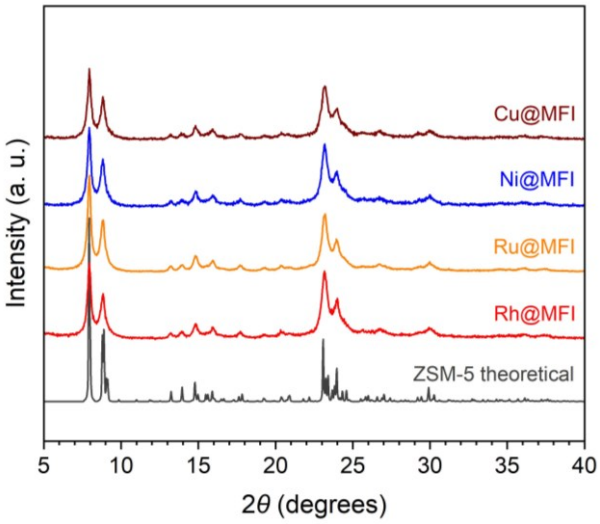

Figure 19. PXRD diffractograms of calculated theoretical ZSM-5 material[10], and prepared X@MFI nanosponge materials, where X = Rh, Ru, Ni, Cu

4.3 Textural properties of prepared materials

Nitrogen sorption was used for the investigation of textural properties of prepared materials. All adsorption isotherms showed below (Figure 20, 22–25) exhibited the combination of type I and type IV(a) isotherm behaviour with H3 hysteresis loop shape confirming disordered mesoporous MFI nanosponge architecture with wedge-shaped and slit-shaped pores.[25]

All samples showed similar textural properties (Table 7–9) with BET surface area (S_{BET}) slightly higher than 550 m^2 g^{-1} and external surface area (S_{EXT}) in the range of

282–302 $m^2\ g^{-1}$, except of the manually impregnated Pt@MFI-MAN sample with S_{BET} of 488 $m^2\ g^{-1}$ and S_{EXT} of 268 $m^2\ g^{-1}$. These results are in agreement with the previous literature reports on this type of materials.[25,27] Decrease in the S_{BET} and S_{EXT} of Pt@MFI-MAN sample could be attributed to the simultaneously ongoing aggregation of ground zeolite particles into looser aggregates of bigger, less milled polycrystallites.

The total pore volumes (V_{TOTAL}) of prepared mechanochemically impregnated catalysts were found between 0.50–0.69 $cm^3\ g^{-1}$, with volumes of micropores (V_{MICRO}) in the range of 0.10–0.12 $cm^3\ g^{-1}$ and volumes of mesopores (V_{MESO}) varying in between 0.38–0.58 $cm^3\ g^{-1}$. Rh@MFI (0.45 $cm^3\ g^{-1}$) and Ru@MFI samples showed slightly different textural properties in contrast to the rest of catalysts with a total pore volume of 0.45 $cm^3\ g^{-1}$ and 0.47 $cm^3\ g^{-1}$, and volume of mesopores 0.32 $cm^3\ g^{-1}$ and 0.35 $cm^3\ g^{-1}$ respectively. This observed phenomenon in the case of Rh- and Ru-impregnated samples was attributed to the use of a new batch of prepared MFI-deGa-calc support, however, does not influence the outcome of material preparation in a significant way. The BJH algorithm indicated for all prepared samples a distribution of mesopore diameters with the centre in the interval of 3.5–4.5 nm.

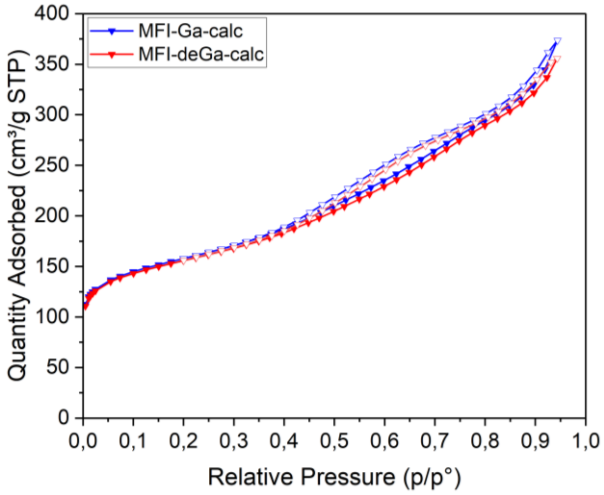

Figure 20. N_2 sorption isotherms of prepared MFI nanosponge supports – MFI-Ga-calc; MFI-deGa-calc

Table 7. Textural properties of prepared MFI nanosponge supports

Support	S_{BET} [$m^2\ g^{-1}$]	S_{EXT} [$m^2\ g^{-1}$]	V_{MICRO} [$cm^3\ g^{-1}$]	V_{MESO} [$cm^3\ g^{-1}$]	V_{TOTAL} [$cm^3\ g^{-1}$]
MFI-Ga-calc	575	297	0.12	0.46	0.58
MFI-deGa-calc	569	286	0.12	0.43	0.55

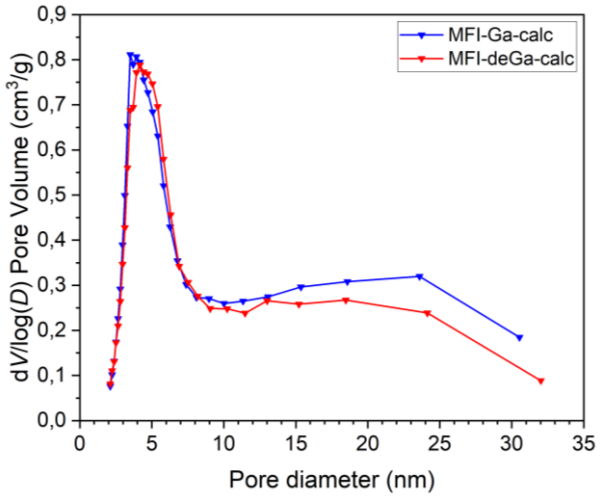

Figure 21. BJH desorption graph of mesopore size distributions of prepared MFI nanosponge supports – MFI-Ga-calc; MFI-deGa-calc

The comparison of textural properties of Pt impregnated MFI nanosponge zeolite samples *via* two different wet impregnation approaches showed relevant differences (Table 8). In the case of the manually impregnated material by using the mortar and the pestle, decrease in a total pore volume and BET surface area, compared to the mechanochemical approach, could be attributed to the formation of bigger, less-compact aggregates of zeolite crystals upon non-even grinding with the pestle. Thus, ball milling led to homogeneous grinding of the support, preventing mentioned aggregation while maintaining milling efficiency.

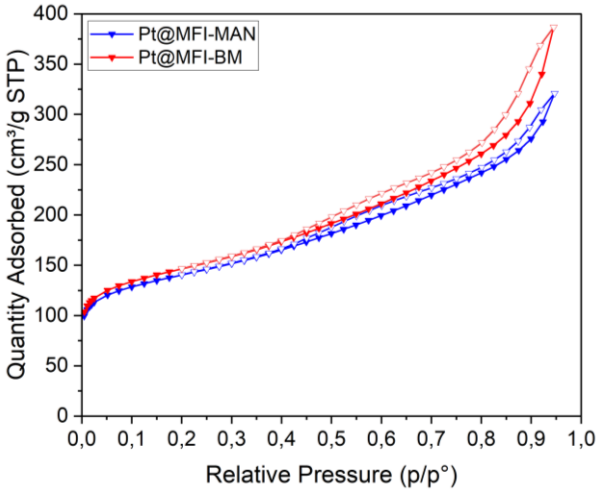

Figure 22. N_2 sorption isotherms of prepared Pt@MFI catalysts (0.5 wt.% of Pt) *via* 2 different impregnation methods: manually – Pt@MFI-MAN, and mechanochemically – Pt@MFI-BM

Table 8. Textural properties of prepared Pt@MFI catalysts (0.5 wt.% of Pt) impregnated manually (Pt@MFI-MAN) and mechanochemically (Pt@MFI-BM)

Catalyst	S_{BET} [$m^2\ g^{-1}$]	S_{EXT} [$m^2\ g^{-1}$]	V_{MICRO} [$cm^3\ g^{-1}$]	V_{MESO} [$cm^3\ g^{-1}$]	V_{TOTAL} [$cm^3\ g^{-1}$]
Pt@MFI-MAN	488	268	0.10	0.38	0.50
Pt@MFI-BM	509	287	0.10	0.48	0.60

Furthermore, N_2 sorption isotherms together with listed textural properties of all mechanochemically impregnated materials are displayed below (Figure 23–24, Table 9). These materials were further used as catalysts for eugenol hydrogenation.

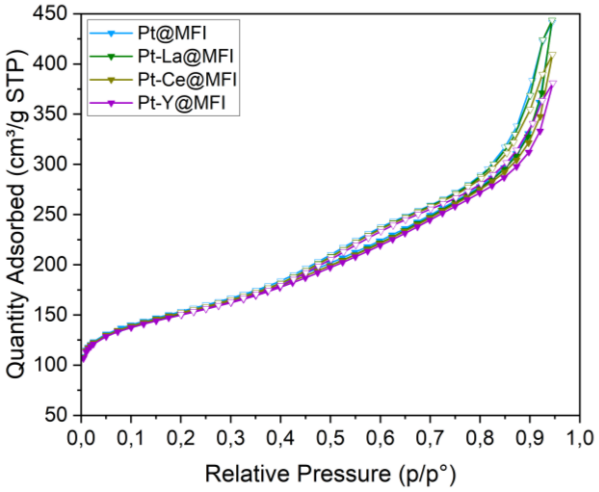

Figure 23. N_2 sorption isotherms of prepared Pt(-RE)@MFI nanosponge materials

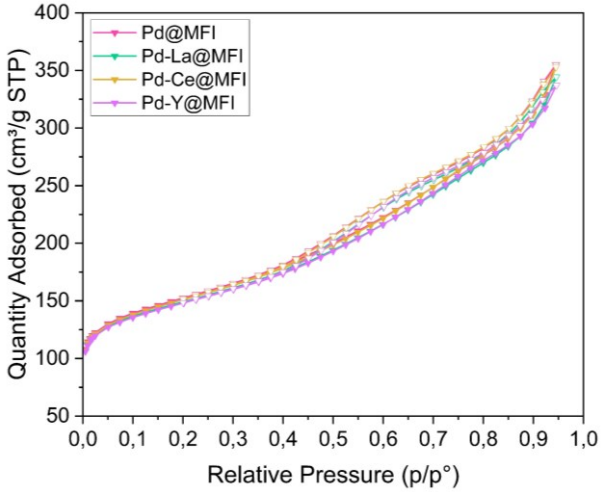

Figure 24. N_2 sorption isotherms of prepared Pd(-RE)@MFI nanosponge materials

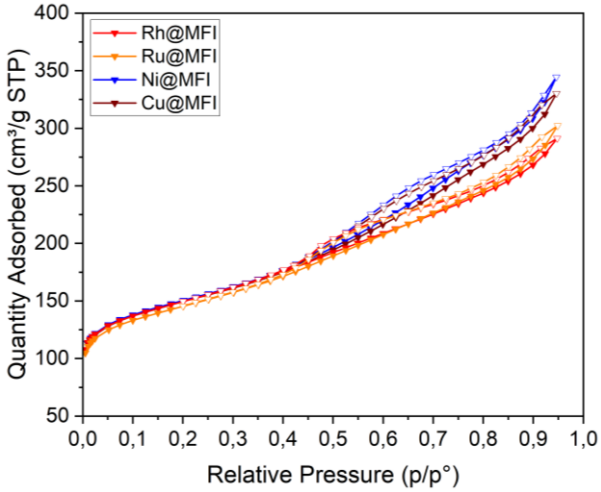

Figure 25. N_2 sorption isotherms and prepared X@MFI nanosponge materials, where X = Rh, Ru, Ni, Cu

Table 9. Textural properties of synthesised catalysts

Catalyst	S_{BET} [$m^2\ g^{-1}$]	S_{EXT} [$m^2\ g^{-1}$]	V_{MICRO} [$cm^3\ g^{-1}$]	V_{MESO} [$cm^3\ g^{-1}$]	V_{TOTAL} [$cm^3\ g^{-1}$]
Pt@MFI	533	297	0.11	0.57	0.68
Pt-La@MFI	525	292	0.11	0.58	0.69
Pt-Ce@MFI	528	290	0.11	0.52	0.63
Pt-Y@MFI	521	285	0.11	0.47	0.59
Pd@MFI	553	298	0.11	0.43	0.55
Pd-La@MFI	542	284	0.11	0.42	0.53
Pd-Ce@MFI	548	296	0.10	0.43	0.55
Pd-Y@MFI	538	282	0.11	0.40	0.52
Rh@MFI	543	284	0.11	0.32	0.45
Ru@MFI	528	289	0.10	0.35	0.47
Ni@MFI	547	283	0.11	0.41	0.53
Cu@MFI	543	282	0.11	0.39	0.52

4.4 Morphology of prepared materials

Scanning electron microscopy images of synthesised supports and prepared impregnated catalysts indicated polycrystalline non-rigid aggregates in morphology of MFI nanosponge materials. Crystallites exhibited coarse-grained surfaces with bristling fibrous edges. Near-circular particles, with diameters ranging from 50 to 500 nm,

accumulated, slabbed and wedged to each other, formed an interparticle mesoporous system (Figure 26, Figure 27).

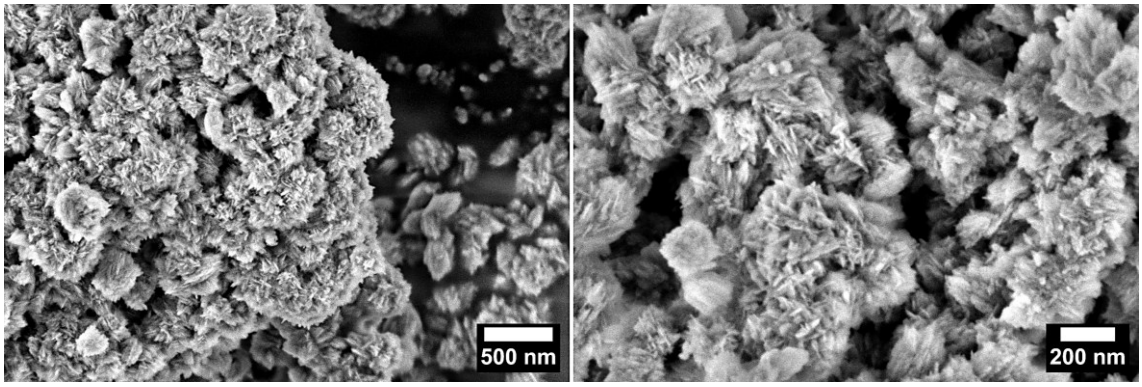

Figure 26. SEM images of gallosilicate MFI nanosponge support – MFI-Ga-calc

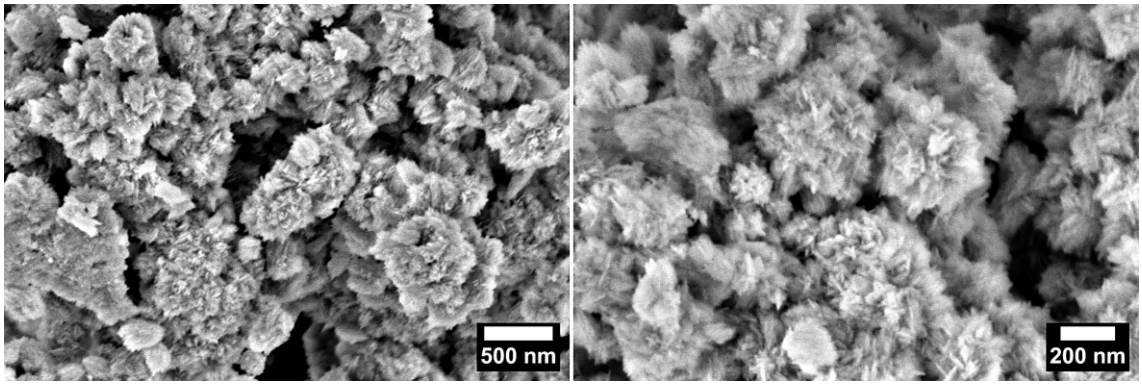

Figure 27. SEM images of degallated gallosilicate MFI nanosponge support – MFI-deGa-calc

Analysis of the morphology of the manually impregnated sample Pt@MFI-MAN and the mechanochemically impregnated sample Pt@MFI-BM showed some differences between the samples. Pt@MFI-BM sample showed crystallites with sharper edges, and reduced crystallite size (Table 10), when compared to manually prepared samples. This phenomenon was attributed to the homogeneous grinding effect of the ball milling. Moreover, agglomeration of polycrystallites into bigger, less-compact aggregates was likewise less significant. Smaller aggregates prevailed in the case of Pt@MFI-BM sample in contrast to the manually impregnated counterpart (Figure 28, Figure 29).

Table 10. Average ($\bar{d}_{cryst}$) and median ($\tilde{d}_{cryst}$) size of crystallites calculated from SEM images of the support – MFI-deGa-calc; manually Pt@MFI-MAN and mechanochemically impregnated sample Pt@MFI-BM

Sample	$\bar{d}_{cryst.}$ [nm]	$\tilde{d}_{cryst.}$ [nm]
MFI-deGa-calc	191	171
Pt@MFI-MAN	119	99
Pt@MFI-BM	84	75

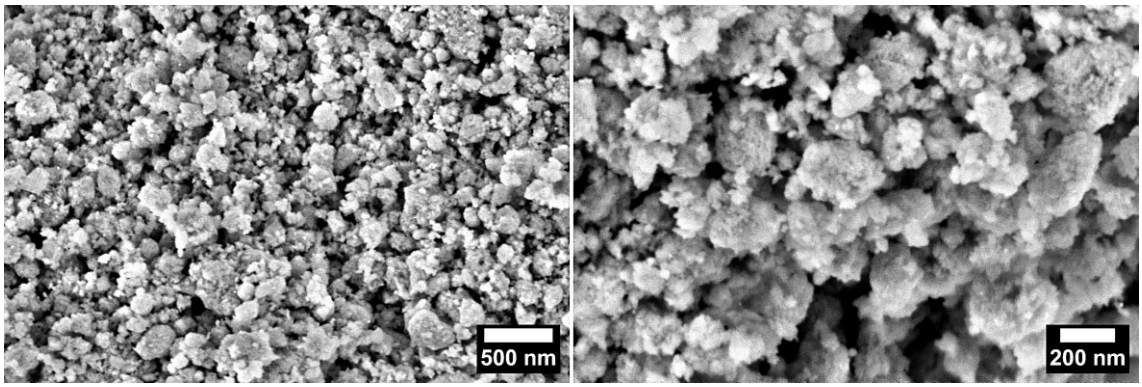

Figure 28. SEM images of manually impregnated sample – Pt@MFI-MAN

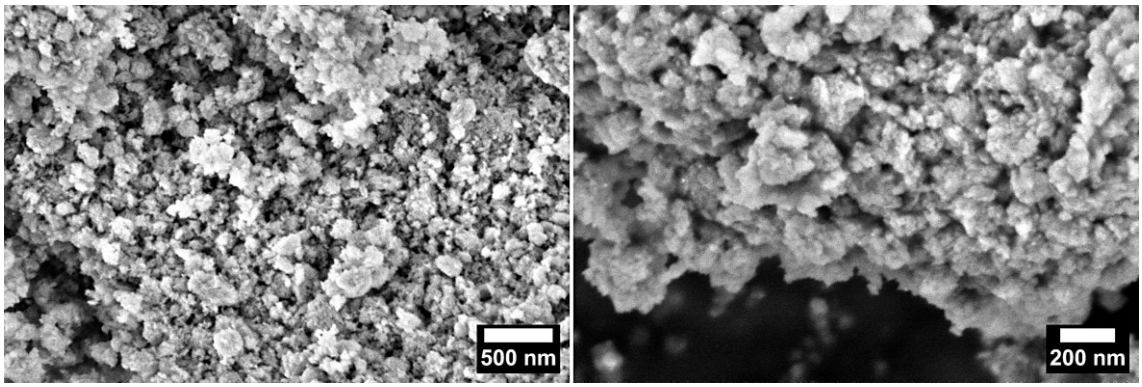

Figure 29. SEM images of mechanochemically impregnated sample – Pt@MFI-BM

As for the rest of mechanochemically impregnated samples, crystallites with similar shapes of reduced sizes and sharper edges were observed. Smaller compact aggregates still dominated. A typical morphology of prepared catalysts was revealed by SEM images of Pt-Ce@MFI nanosponge sample (Figure 30). No big metal NPs anchored onto the external surface of the zeolite were detected by the BSE detector. This fact indicated metal nanoparticle size distributions with maxima below 10 nm in diameter and their uniform dispersion throughout the support surface.

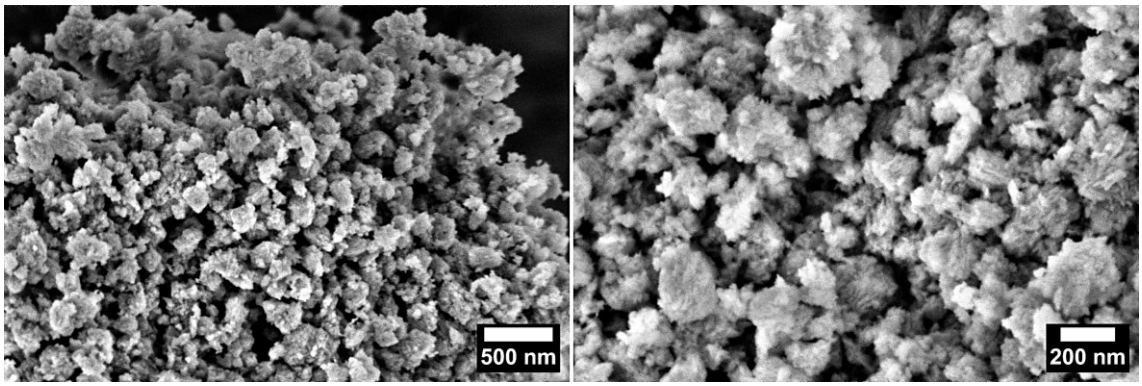

Figure 30. SEM images of mechanochemically impregnated Pt-Ce@MFI sample indicating the morphology of prepared catalysts

In the case of Rh- and Ru-impregnated samples, SEM images revealed the similarities in morphology to the support morphology before the ball milling. However, poorly defined crystallites of spike-shaped outgrowths were observed wedged together, forming big agglomerates (Figure 31). This observation, insignificant for subsequent catalytic experiments, resulted from the use of a different batch of the zeolite as the support.

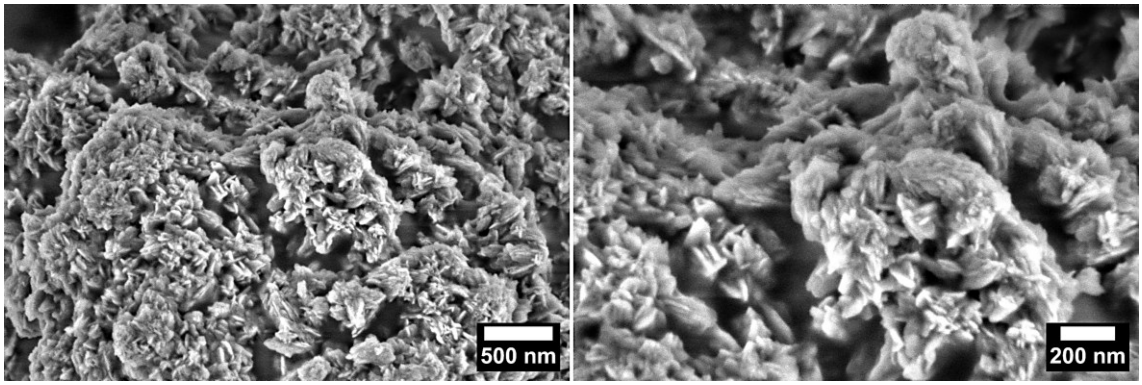

Figure 31. SEM images of mechanochemically impregnated Ru@MFI sample indicating an altered morphology

4.5 Zeolite structure and metal particle size distribution analysis

Images obtained by scanning transmission electron microscope confirmed nanosponge architecture of prepared MFI zeolites as supports. Interconnected disordered network of MFI nanolayers was visible, especially in thin peripheral areas of zeolite crystals scattered and deposited on thin carbon layer on the copper grid. Moreover, MFI topology of the prepared support was clearly recognisable (Figure 32).

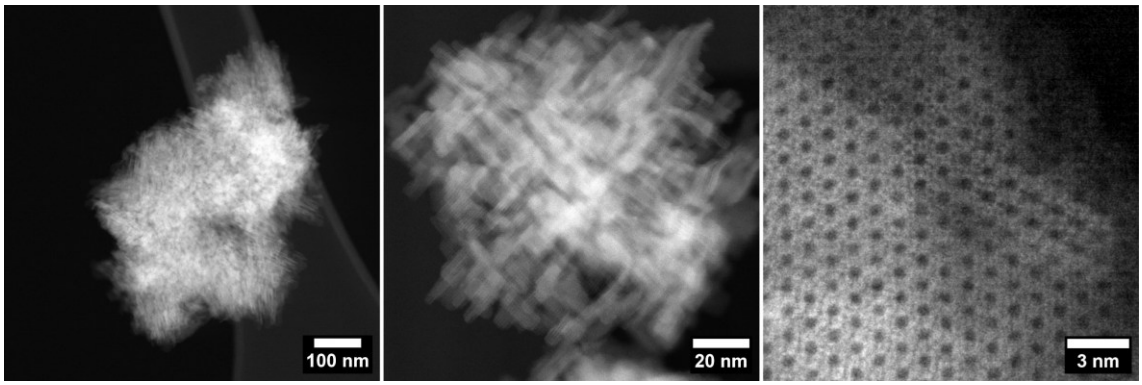

Figure 32. STEM images of prepared support – MFI-deGa-calc of nanosponge architecture visible in the left and middle images, and MFI topology of the support depicted in the right image

All the metal-impregnated samples were imaged by STEM microscopy. The dispersion of NPs was confirmed by imaging in a low magnification mode (≤500 thousands). The main focus of STEM imaging revolved around metal species anchored to the external surface of zeolite, particularly with an emphasis on nanoparticles size distribution.

Metal particle size distribution (PSD) analysis was conducted based on the images with a sufficient magnification (≥1 million) and high resolution. During PSD analysis, NPs were approximated to have roughly spherical shapes. NPs with recognisable sharp edges were used for the measurements to provide precise analysis. The images analysed were representative of each sample, and the PSD profiles were based on a sufficiently large number of measured NPs to ensure statistical significance.

As for the comparison of manual and mechanochemical wet impregnation approach, particle size distribution analysis based on the STEM images of Pt@MFI-MAN and Pt@MFI-BM samples (0.5 wt.% of Pt) indicated significant differences in profiles and positions of maxima of PSD histograms (Figure 33, Figure 34).

In the case of manually impregnated sample, PSD analysis showed the presence of two populations of metal NPs (2 maxima at approximately 2 nm and 9 nm) with the biggest NPs reaching almost 15 nm in their diameters. On the contrary, much uniform profile with only 1 maximum at the diameter of 1.5 nm was observed in the PSD histogram of the ball milled sample with the biggest NPs measuring roughly 10 nm.

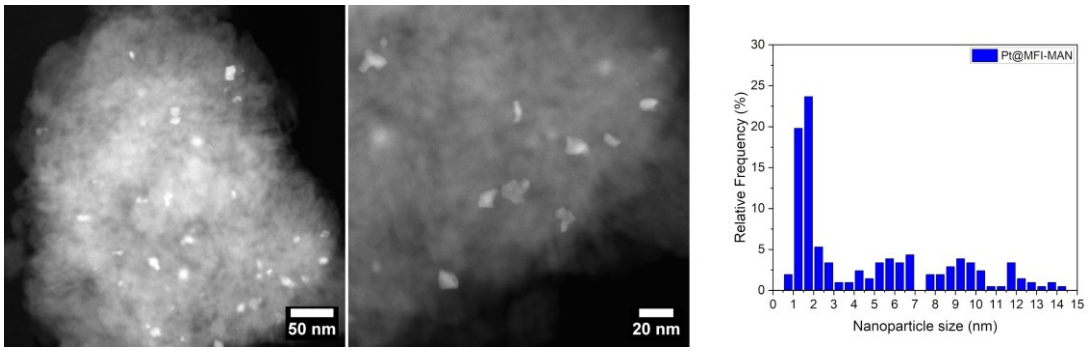

Figure 33. STEM images of Pt@MFI-MAN sample with particle size distribution analysis. In PSD histogram 2 maxima were observed at around 2 nm and 9 nm in nanoparticles diameters

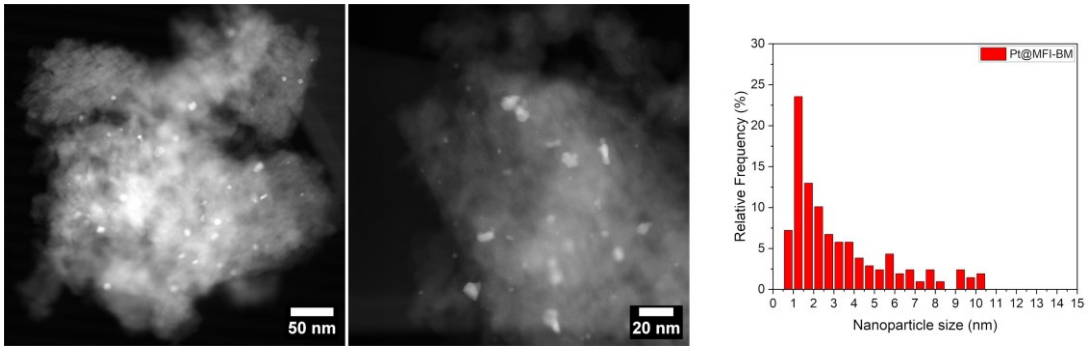

Figure 34. STEM images of Pt@MFI-BM sample with particle size distribution analysis. PSD histogram exhibited a narrower profile with 1 maximum observed at around 1.5 nm in nanoparticles diameters

STEM imaging was performed also for all of the catalysts prepared by mechanochemical approach. Loadings of metals and RE elements in all further prepared materials were around 1 wt.% for each element separately (Figure 35–46). Simultaneous mechanochemical incorporation of RE elements as metal promoters alongside the primary metal resulted in noticeable lesser susceptibility of NPs towards sintering. This led to the formation of smaller NPs with particle diameter maxima in the range of 1.1–1.4 nm and an additional improved dispersion compared to monometallic samples with generally bigger NPs with diameter maxima in the range of 1.4–2.0 nm.

An exceptionally fine PSD, with maximum around 1.1 nm with a big fraction (almost 40 %) of particles of such diameter and narrow PSD profile exhibited the Rh-impregnated sample (Figure 43). The worst, most irregular PSD relative to the series of the mechanochemically impregnated materials indicated the Ni-impregnated sample with maximum close to 2.0 nm with a relatively broad profile (Figure 46). Differences in PSD arose due to the NPs' size strongly dependent on the constituting metal, the stabilising support (diverse metal-support interactions), and the metal precursor used.

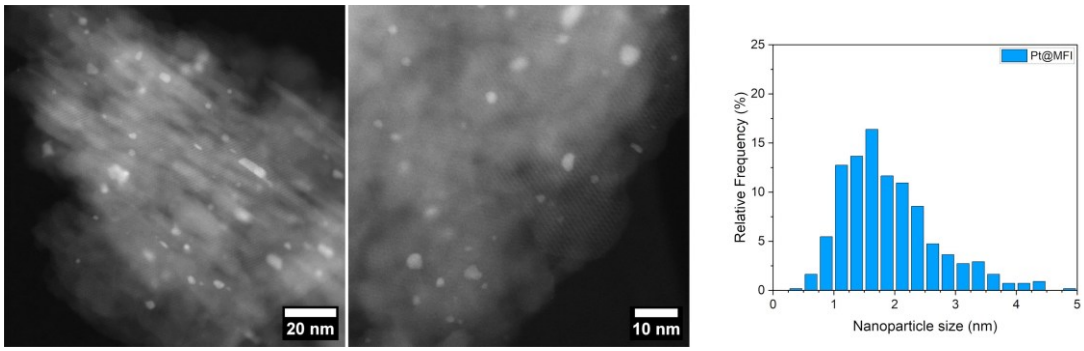

Figure 35. STEM images of Pt@MFI sample of PSD with maximum around 1.7 nm in diameter

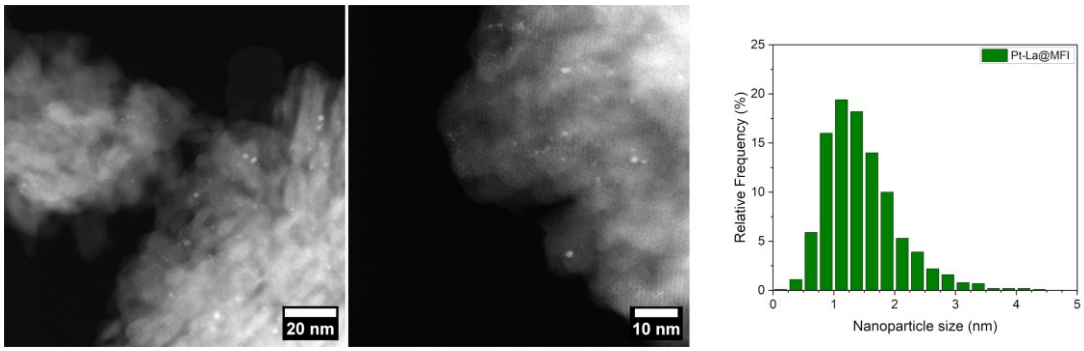

Figure 36. STEM images of Pt-La@MFI sample of PSD with maximum around 1.3 nm in diameter

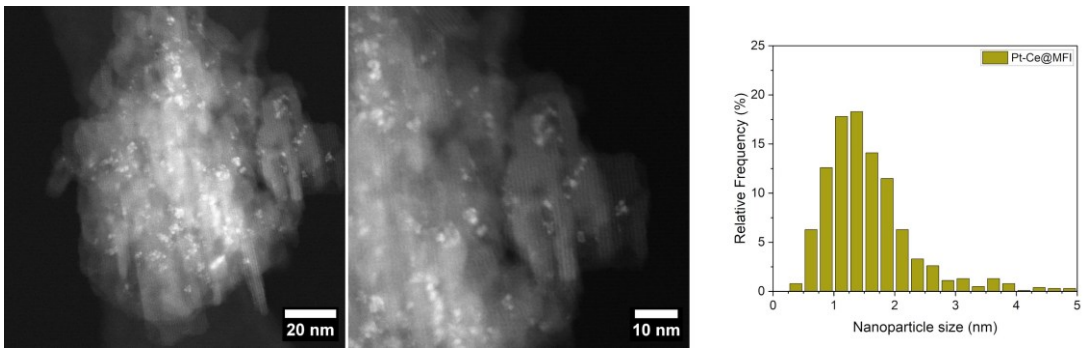

Figure 37. STEM images of Pt-Ce@MFI sample of PSD with maximum around 1.4 nm in diameter

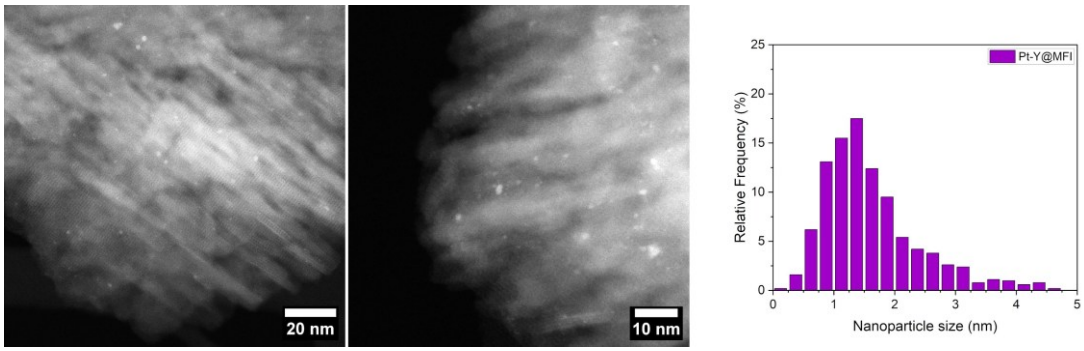

Figure 38. STEM images of Pt-Y@MFI sample of PSD with maximum around 1.4 nm in diameter

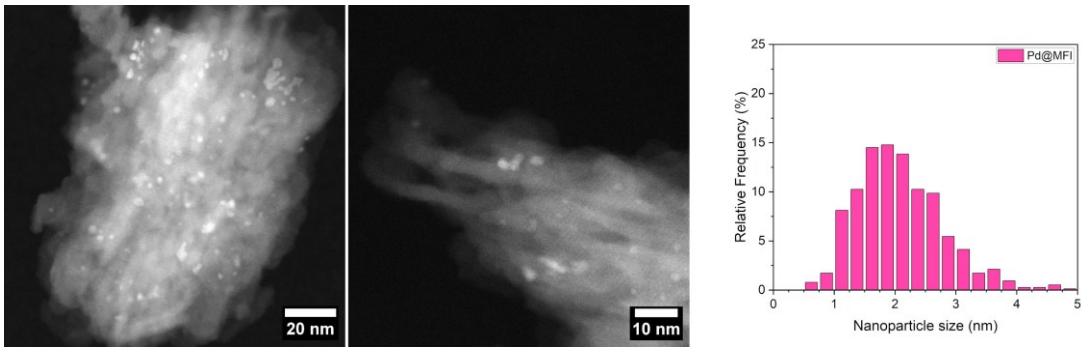

Figure 39. STEM images of Pd@MFI sample of PSD with maximum around 1.9 nm in diameter

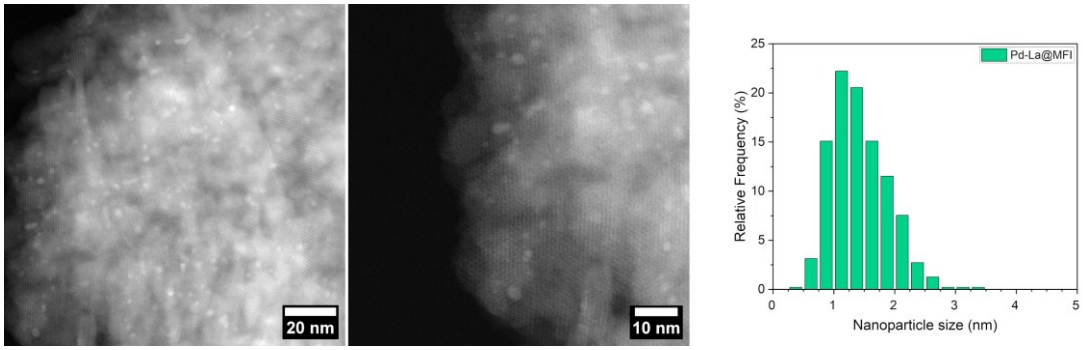

Figure 40. STEM images of Pd-La@MFI sample of PSD with maximum around 1.3 nm in diameter

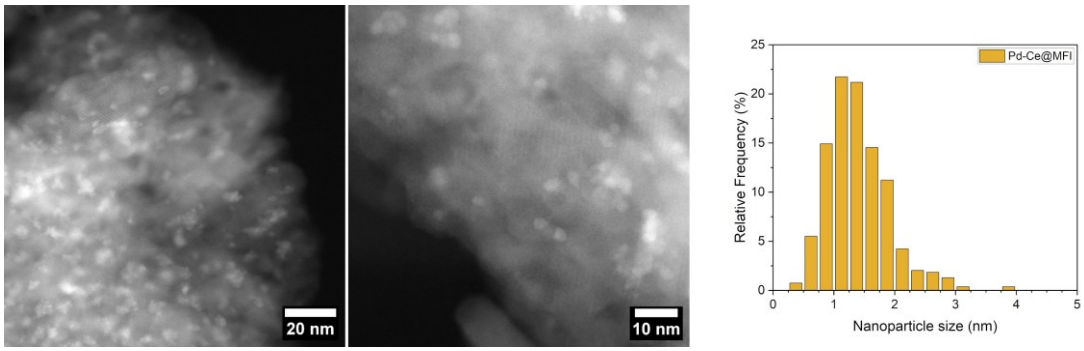

Figure 41. STEM images of Pd-Ce@MFI sample of PSD with maximum around 1.3 nm in diameter

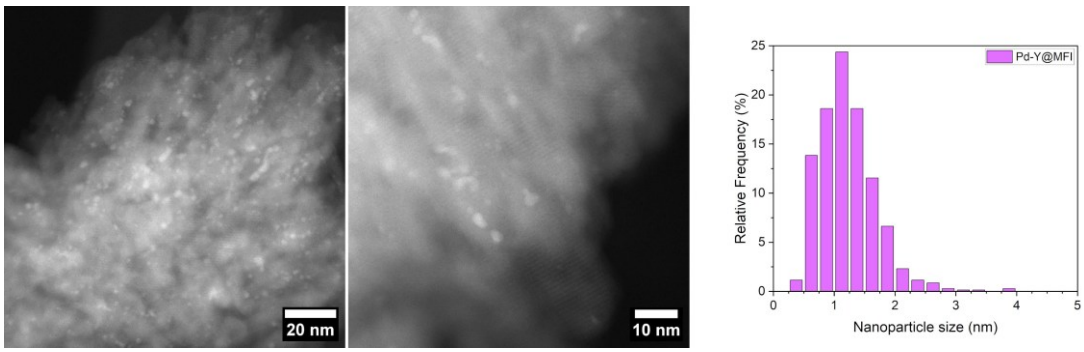

Figure 42. STEM images of Pd-Y@MFI sample of PSD with maximum around 1.2 nm in diameter

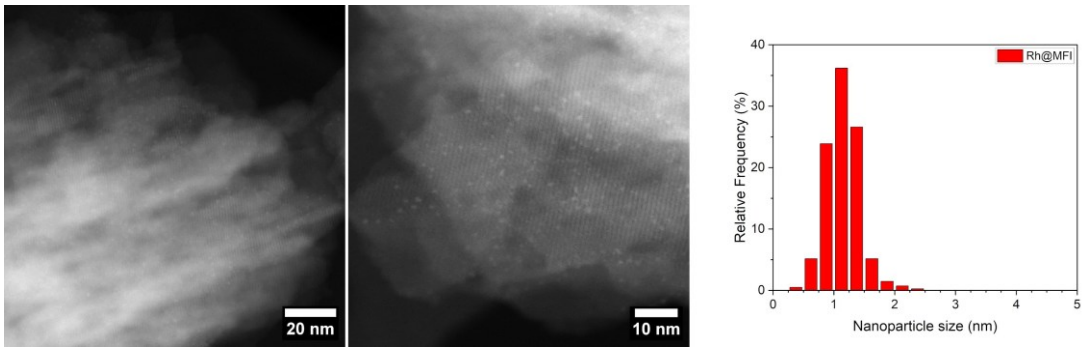

Figure 43. STEM images of Rh@MFI sample of PSD with maximum around 1.1 nm in diameter

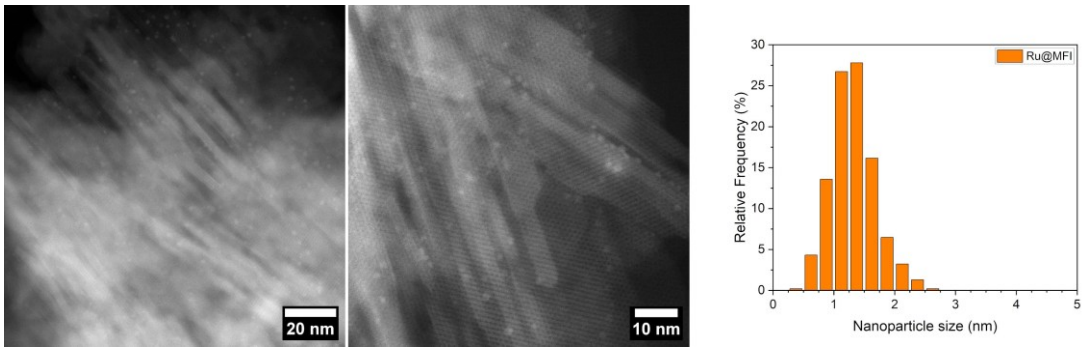

Figure 44. STEM images of Ru@MFI sample of PSD with maximum around 1.4 nm in diameter

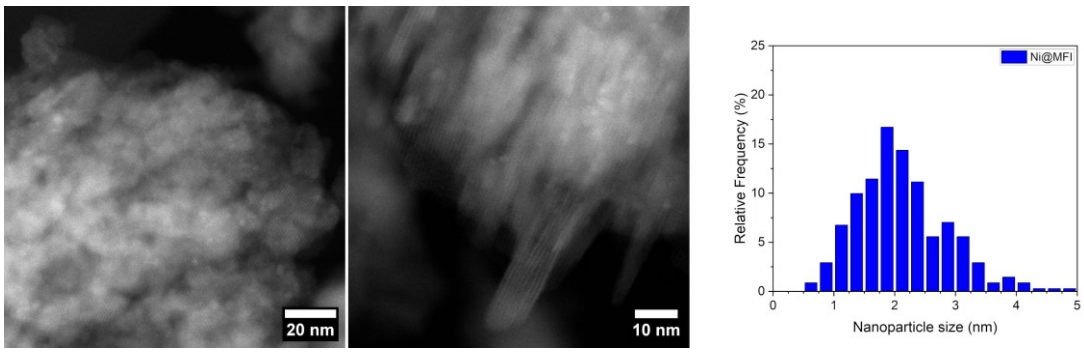

Figure 45. STEM images of Ni@MFI sample of PSD with maximum around 2.0 nm in diameter

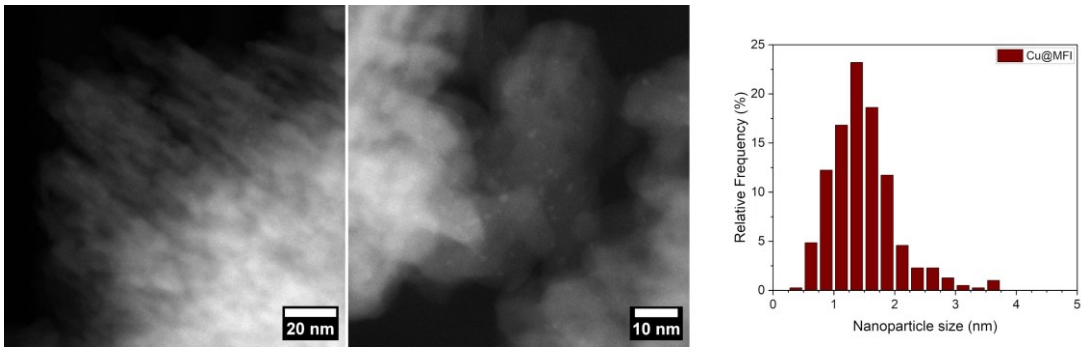

Figure 46. STEM images of Cu@MFI sample of PSD with maximum around 1.4 nm in diameter

Elemental mapping of prepared materials was performed by STEM-EDS imaging. The analysis targeted the uniformity of dispersion of mono- and bimetallic species anchored onto zeolite crystallites together with NPs' elemental composition. Both the gallosilicate MFI nanosponge (MFI-Ga-calc) and its degallated form (MFI-deGa-calc) were analysed by STEM-EDS, confirming the Si/Ga ratio of ~50 for the gallosilicate and ≥150 for the degallated MFI zeolite. These results suggested that the majority of Ga was removed from the zeolite framework during the degallation using nitric acid, and the remaining traces could be neglected.

The comparison of the dispersion of Pt NPs stabilised at the zeolite by wet impregnation achieved both manually and mechanochemically showed a uniform dispersion of metal species. As previously shown and discussed, monometallic Pt@MFI materials contained also bigger Pt NPs (approximately 5–15 nm in diameter). These are visible and represented as local clusters of cyan dots in the Pt elemental maps (Figure 47, Figure 48) confirming the efficiency of STEM-EDS mapping. Nevertheless, this method lacks sufficient resolution to clearly detect smaller clusters; however, it demonstrates the presence of well-dispersed metal species in the materials.

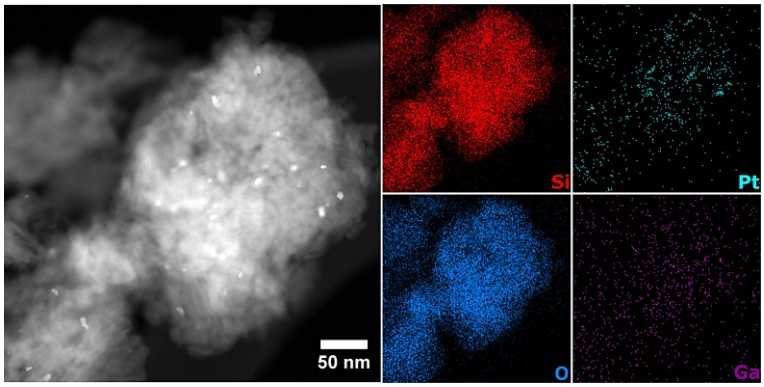

Figure 47. STEM images with corresponding EDS elemental maps of Pt@MFI-MAN sample

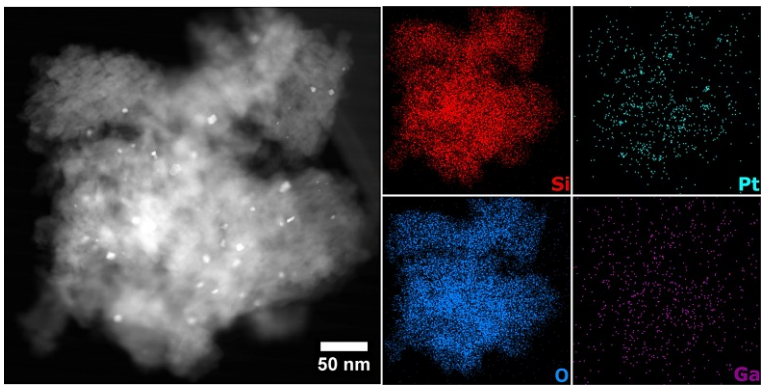

Figure 48. STEM images with corresponding EDS elemental maps of Pt@MFI-BM sample

Furthermore, STEM-EDS imaging and analysis was performed for all of the mechanochemically wet-impregnated catalysts. In all the cases, uniform dispersions of small metal species were achieved with no visible particles of RE element oxides being formed, which aligned with previously analysed PXRD patterns. Moreover, RE elements were well-distributed throughout the zeolite crystallites, which suggested that produced nanoparticles were indeed bimetallic. In the original work of Ryoo *et al.*, authors claimed that these nanoparticles were bimetallic alloys.[7] Herein, I do not present any direct evidence for the presence of alloys, nevertheless, elemental mappings showed uniform dispersions of metals and RE elements within the samples. Due to the limited space in this work, these observations in elemental compositions of mono- and bimetallic NPs in the prepared nanocomposites are indicated by the STEM image with corresponding EDS elemental maps of the Pt-Ce@MFI sample selected as a representative material (Figure 49).

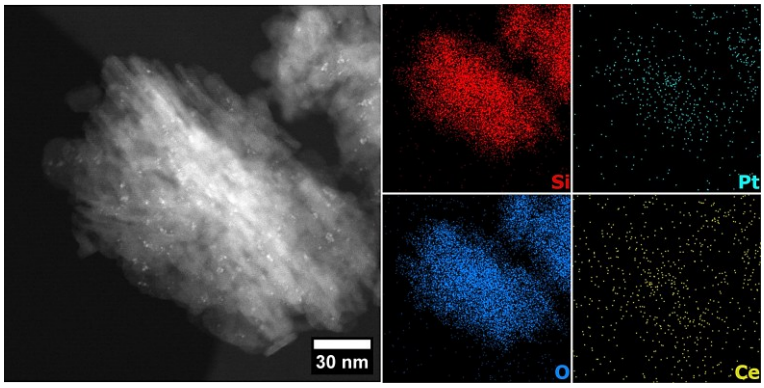

Figure 49. STEM images with corresponding EDS elemental maps of Pt-Ce@MFI sample indicating uniform dispersions of stabilised mono- and bimetallic species of prepared catalysts

4.6 Hydrogenation of eugenol

All mechanochemically wet impregnated catalysts were tested in a catalytic hydrogenation reaction of eugenol as the substrate. A typical reaction mixture was composed of 1.55 ml of eugenol (10 mmol), 0.7 ml of *n*-dodecane and 36 ml of 2-propanol as a solvent. 100 mg of the pre-reduced catalyst was added.

Prior to the catalytic experiment, the optimisation of the reaction conditions was executed. In particular, the focus was placed on the selection of the right solvent to sufficiently dissolve the reactant – eugenol, and the internal standard – *n*-dodecane. Additionally, an important factor for catalyst functionality is its proper dispersion in the reaction mixture. Thus, the catalyst wettability had to be controlled. This ensured a

good contact of the catalyst with the reaction mixture components and prevented material from sticking to the walls of the batch reactor above the reaction mixture level. Pt@MFI nanosponge material (1 wt.% of Pt) was selected as the catalyst for the optimisation process. The results of the optimisation are listed in Table 11, that includes observations and comments for each solvent.

Considering the results of the optimisation analysis, 2-propanol was selected as the solvent for subsequent catalytic experiments. However, sampling of the reaction mixture remained challenging. Consequently, the assurance that the composition of collected samples precisely matched the composition of the actual reaction mixture was questionable. Thus, the emphasis was placed on the sample collected after 6 h directly from the opened batch reactor.

Table 11. Results of the prior optimisation of the reaction conditions for eugenol hydrogenation primarily focusing on the selection of the right solvent: solvent used, eugenol conversion (x_{EUG}) reached after 6 h, comments and observations regarding the experiment execution and the outcome

Solvent	x_{EUG} [%]	Comments and observations
1-Hexanol	25–35	• Insufficient wettability of catalysts • Lesser activity • Ideal sampling
Ethyl acetate	61–93	○ Wettability of catalysts ○ Higher activity, varying conversions ○ Ideal sampling
2-Propanol	51–53	• Wettability of catalysts • Average activity, steady conversions • Challenging sampling

The following analysis and evaluation of the catalytic performance of the mechanochemically prepared catalysts showed the formation of variously hydrogenated and hydrodeoxygenated products. Obtained products were identified based on the MS spectra acquired from GC-MS measurements. The summary of results of catalytic experiments is presented in Table 12 and Table 13. In total, 3 key variables were monitored: the eugenol conversion x_{EUG}, the yields of individual products y_i, and the selectivity towards them s_i, all reached after 6 h.

A complex scheme of hydrogenation and hydrodeoxygenation (HDO) reaction pathways was proposed (Figure 50). Products, namely PPOL, PCHO, and PCHOL are onwards grouped and labelled together as HDO since represent the only HDO products.

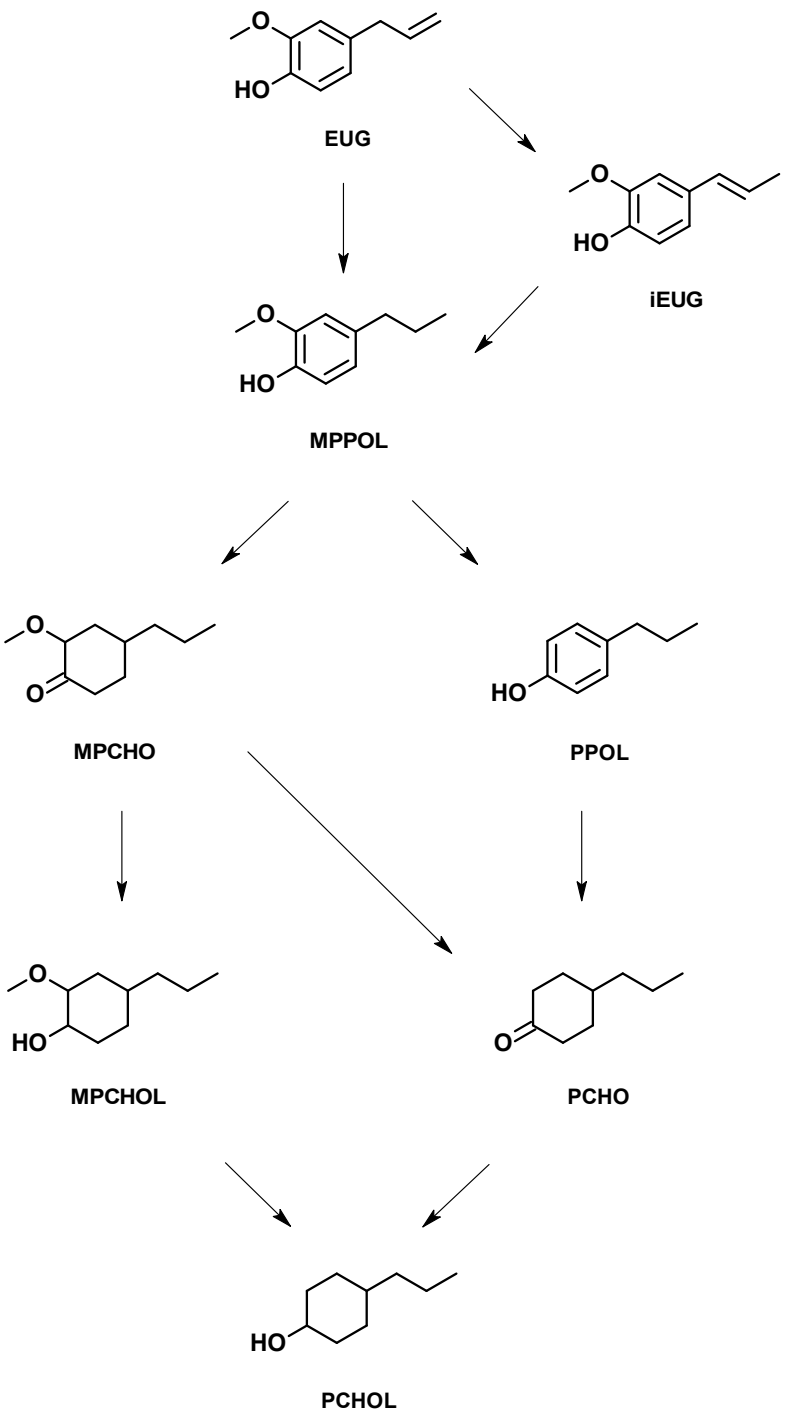

Figure 50. Suggested complex scheme of catalytic hydrogenation and hydrodeoxygenation reaction pathways in the process of eugenol conversion[8,45,48]

At first, a blank reaction without a catalyst used was performed. After 6 h of catalytic experiment, the eugenol conversion of 4 % was achieved indicating some negligible hydrogenation reaction ongoing without the catalyst. This might be attributed to the setup, mainly the reaction vessel or the equipment effects, e.g., traces of active metals embedded in the stainless-steel stirrer or the reactor itself. Similar results were obtained, when the support (MFI-deGa-calc) with no metals incorporated was used as the catalyst, confirming blank experiment.

When Pt@MFI sample was used as the catalyst, only 53 % of eugenol conversion was achieved with 77 % selectivity towards hydrogenation of the terminal double bond of eugenol to yield MPPOL after 6 h. Retained similar values of selectivity towards MPPOL (80–83 %) were reached in the case of Pt(-RE)@MFI as catalysts with an enhanced conversion of eugenol reaching 100 % in just 4 h. The only byproduct formed was iEUG.

Pd-impregnated samples as catalysts enabled reaching full eugenol conversions in just 1 h with 100 % selectivity towards MPPOL. In the case of bimetallic Pd-impregnated catalysts, the selectivity altered with an arising formation of further hydrogenated and hydrodeoxygenated products. Interestingly, when Pd-La@MFI sample was used as the catalyst, the yield of MPCHOL was increased to 6 % in contrast to 0.5 % as in the case of Pd-Ce@MFI and Pd-Y@MFI catalysts. Moreover, from a total yield of HDO products equalling 2 %, yields of both PPOL and PCHOL reached 0.8 %. No iEUG was formed at all.

The reaction with Rh@MFI as the catalyst showed similar conversion and selectivity as in the case of Pd-Ce@MFI and Pd-Y@MFI catalysts. Notably, the highest selectivity towards MPCHOL and HDO products was reached with Ru@MFI catalyst, in particular, 8 % selectivity towards MPCHOL and 7 % selectivity in total towards HDO products (6 % towards PCHOL and 1 % towards PPOL). Furthermore, 100 % eugenol conversion was achieved using the Ni@MFI catalyst after 6 h, with nearly full conversion attained within 1 h. Lastly, Cu@MFI catalyst did not show any activity, providing similar results as for the blank reaction. To investigate the possible causes of such behaviour, STEM imaging and EDS analysis of the spent Cu@MFI catalyst was performed. It confirmed no leaching of Cu species; moreover, no evidence of metal sintering nor indication of catalyst coking was observed. Such low catalytic activity of

the Cu@MFI sample could possibly be caused by a fast deactivation of the catalyst upon the oxidation of Cu NPs that might have occurred during the transfer of the reduced material to the reaction mixture. This will be investigated in the future, e.g., by in-situ reduction of the catalyst.

To summarise the catalytic results, high catalytic activity of the prepared materials was observed. The only exception was an inactive Cu@MFI material. Based on the decrease in hydrogenation and hydrodeoxygenation activities, the catalysts were ordered into the following order: Ru > Pd-La >> Pd-Ce ≈ Pd-Y > Rh > Pd > Ni > Pt-La ≈ Pt-Ce ≈ Pt-Y > Pt >> Cu. As for the HDO process, only demethoxylation was observed with no dehydroxylation (removal of −OH group) occurring. The highest HDO activity was obtained in the case of Ru@MFI sample. This observation confirmed a significant affinity of Ru metal to bind oxygen. Moreover, the decrease in deoxygenation activities of the catalysts observed in this study aligns with the trend of metal oxophilicity (Ru > Rh > Pd ≈ Pt) reported in the articles by Bjelić[46] and Tan[8,78]. Nevertheless, the simultaneous incorporation of RE elements as metal promoters with PGM (especially Pd) apparently influenced the deoxygenation trend by forming catalytically active sites with an enhanced oxophilicity and, hence, promoted the formation of HDO products. Another key factor potentially influencing the catalytic activity and selectivity of the bimetallic catalysts is the modification of the support's acidic properties and its synergistic effect with the reductive properties of the metal species. The change in acidity could be induced by the incorporation of light RE elements with their empty 4f orbitals.[79] Acidity is also likely to play an important role in the eugenol hydrogenation reaction. Investigation of this aspect lies beyond the scope of this thesis; however, it is planned for a future work.

In addition, by comparing the yield differences $y_{MPCHOL}-y_{PCHOL}$ and $y_{PPOL}-y_{PCHOL}$, it can be roughly assumed that the removal of the eugenol methoxy group $-OCH_3$ is easier from the aromatic ring than from the saturated compounds. Particularly, as for Ru@MFI catalyst, the values of $y_{MPCHOL}-y_{PCHOL}$ and $y_{PPOL}-y_{PCHOL}$ equalled 2 % and −5 % respectively. These values indicated the excess of MPCHOL as a saturated methoxylated compound and the deficiency of PPOL as an aromatic demethoxylated compound compared to PCHOL as a both saturated and demethoxylated compound. This assumption agreed with the results of the work reported by Bjelić[8].

Overall, the activation energies for hydrogenation reactions are typically lower than for deoxygenation reactions. Therefore, higher temperatures (200–450 °C) and elevated pressures (2–30 MPa) are required to achieve deoxygenation reactions with a desirable selectivity. For the future work, the catalytic experiments are planned to be performed at harsher reaction conditions (elevated temperatures, e.g., 225 °C) to promote a desirable HDO process.

Table 12. The results of catalytic experiments with mechanochemically prepared samples used as catalysts: eugenol conversion x_{EUG} reached after 6 h, yield of product y_i after 6 h

Catalyst	x_{EUG} [%]	y_{iEUG} [%]	y_{MPPOL} [%]	y_{MPCHO} [%]	y_{MPCHOL} [%]	y_{HDO} [%]
none	4.0	<1	3.6	-	-	-
Pt@MFI	53	12	41	-	-	-
Pt-La@MFI	100	20	83	-	-	-
Pt-Ce@MFI	100	19	83	-	-	-
Pt-Y@MFI	100	23	80	-	-	-
Pd@MFI	100	-	100	-	-	-
Pd-La@MFI	100	-	89	<1	6	2
Pd-Ce@MFI	100	-	98	<0.5	0.5	<0.5
Pd-Y@MFI	100	-	98	<0.5	0.5	<0.5
Rh@MFI	100	-	98	<0.5	<0.5	<0.5
Ru@MFI	100	-	85	<0.5	8	7
Ni@MFI	100	-	100	-	-	-
Cu@MFI	4.9	<1	4.2	-	-	-

Table 13. The results of catalytic experiments with mechanochemically prepared samples used as catalysts: eugenol conversion x_{EUG} reached after 6 h, selectivity towards product s_i after 6 h

Catalyst	x_{EUG} [%]	s_{iEUG} [%]	s_{MPPOL} [%]	s_{MPCHO} [%]	s_{MPCHOL} [%]	s_{HDO} [%]
none	4.0	<25	90	-	-	-
Pt@MFI	53	23	77	-	-	-
Pt-La@MFI	100	20	83	-	-	-
Pt-Ce@MFI	100	19	83	-	-	-
Pt-Y@MFI	100	23	80	-	-	-
Pd@MFI	100	-	100	-	-	-
Pd-La@MFI	100	-	89	<1	6	2
Pd-Ce@MFI	100	-	98	<0.5	0.5	<0.5
Pd-Y@MFI	100	-	98	<0.5	0.5	<0.5
Rh@MFI	100	-	98	<0.5	<0.5	<0.5
Ru@MFI	100	-	85	<0.5	8	7
Ni@MFI	100	-	100	-	-	-
Cu@MFI	4.9	<20	86	-	-	-

5 Conclusions

In this work, a novel class of heterogeneous catalysts of mechanochemically impregnated, stabilised metal nanoparticles at the zeolite MFI nanosponge was investigated. Mechanochemical approach not only automatised and sped up the impregnation process but also ensured a more uniform particle size distribution than the manual synthesis. I was able to provide comprehensive analysis of catalytic activity of various metal nanoparticles using eugenol hydrogenation as a model reaction for lignin valorisation. Stabilisation of metal species and RE elements at the zeolite led to the nanocomposites possessing uniform PSD profiles, featuring small nanoparticles (0.5–4.0 nm). In addition, bimetallic catalysts with a smaller metal NPs exhibited an enhanced catalytic activity and selectivity, positioning them as promising future contenders for HDO of eugenol.

In total, a series of 12 catalysts was prepared using a degallated MFI zeolite with nanosponge architecture as a support, incorporating 1 wt.% of primary metals (Pt, Pd, Rh, Ru, Ni, Cu) and, where applied, an additional 1 wt.% of RE elements (La, Ce, Y) *via* wet impregnation. The catalysts contained various stabilised metal NPs, and their catalytic performance was screened in the model reaction.

The MFI gallosilicate support was successfully synthesised and degallated to create silanol nests, crucial for further NPs stabilisation, as confirmed by PXRD, N_2 sorption, SEM, and STEM. Both manual and mechanochemical wet impregnation of metal species preserved zeolite structure and crystallinity. Mechanochemical approach led to the formation of more uniform, smaller Pt NPs (with only 1 maximum at around 1.5 nm in diameter) compared to manual impregnation (2 maxima at 2 nm and 9 nm), highlighting its potential as an alternative approach for stabilising metal NPs in heterogeneous catalysts.

Mechanochemistry was selected as an optimal impregnation approach and further applied to prepare catalysts with co-incorporated RE elements, resulting in smaller, better-dispersed NPs (maxima at 1.1–1.4 nm) compared to monometallic samples (1.4–2.0 nm). In general, the materials displayed a uniform PSD of small mono- and bimetallic species, providing an optimal balance between their surface area and stability to be exploited in catalytic processes.[80]

The catalytic behaviour of the prepared catalysts was screened in a model reaction for lignin valorisation process – eugenol hydrogenation. Optimisation of the reaction conditions led to the selection of 2-propanol as the solvent. Consecutively, the analysis of the catalytic performance of materials displayed the formation of variously hydrogenated and hydrodeoxygenated products. A complex scheme of hydrogenation and HDO reaction pathways was proposed based on the formed products.

The results of catalytic experiments indicated a high catalytic activity of the ball milled samples. In terms of the hydrogenation and hydrodeoxygenation activities, the catalysts followed this order: Ru > Pd-La >> Pd-Ce ≈ Pd-Y > Rh > Pd > Ni > Pt-La ≈ Pt-Ce ≈ Pt-Y > Pt >> Cu. As for HDO products, only demethoxylation was observed with no evidence of dehydroxylation occurring. The highest HDO catalytic activity was observed in the case of Ru-impregnated sample, highlighting Ru metal significant affinity for binding oxygen. Furthermore, the incorporation of RE elements as metal promoters with PGM (mainly Pd) influenced the deoxygenation pathway, enhancing the formation of HDO products. In addition, by comparing the yield differences $y_{MPCHOL}-y_{PCHOL}$ and $y_{PPOL}-y_{PCHOL}$, it was estimated that a removal of the methoxy group from eugenol molecule was easier when attached to an aromatic ring than to saturated compounds. The assumption aligned with the findings reported by Bjelić[8].

In conclusion, the mechanochemically prepared materials showed an interesting selective hydrogenation and hydrodeoxygenation catalytic behaviour in the eugenol conversion reaction. Although, the hydrogenation of the eugenol terminal double bond was a dominant reaction process, Ru-impregnated sample demonstrated the highest HDO catalytic activity and selectivity. Additionally, bimetallic species anchored to the zeolite displayed an enhanced catalytic activity or improved selectivity towards HDO products compared to their monometallic counterparts, positioning them as potential candidates for further eugenol HDO.

Future investigations could target the determination of specific catalytic activities of the materials, such as turnover frequencies, at defined eugenol conversions by reducing the amount of a catalyst used. Further emphasis could be directed towards examining how the presence of RE elements affects the acidic properties of the zeolite and, in turn, influences the formation of HDO products during eugenol hydrogenation. Moreover, the focus could be placed on enhancing the selectivity towards HDO by increasing the

reaction temperature (e.g., ≥225 °C). The catalytic performance of prepared materials could be evaluated in another model reaction using a dimeric compound 2-phenoxy--1-phenylethanol as a substrate, owing to the presence of the β–O–4 linkage in the molecule. Last but not least, different demetallated zeolites MFI nanosponge could be explored as supports, e.g., boro- or aluminosilicates, for stabilisation of mono- and bimetallic species. This would improve the cost-effectiveness of the presented approach.

While direct studies on (platinum group metal)-(rare-earth element) bimetallic catalysts for lignin valorisation are limited, a knowledge gap persists in comprehending their full catalytic potential. So far, existing research indicates that such combinations of metals as catalytically active species could enhance lignin conversion, depicting the need for further investigations to bridge this gap. This research provides a desired insight into the synthesis, characterisation and the catalytic performance of such materials that could be further employed for the preparation of second-generation catalysts for lignin valorisation.

6 References

1. Ragauskas, A. J. *et al.* Lignin Valorization: Improving Lignin Processing in the Biorefinery. *Science* 344, 1246843 (2014).
2. Ročnik, T. *et al.* Catalytic lignin valorisation by depolymerisation, hydrogenation, demethylation and hydrodeoxygenation: Mechanism, chemical reaction kinetics and transport phenomena. *Chem. Eng. J.* 448, 137309 (2022).
3. Smeets, S. & Zou, X. Zeolite Structures. in *Zeolites in Catalysis: Properties and Applications* (eds. Čejka, J. et al.) 37–72 (The Royal Society of Chemistry, 2017).
4. Li, A. *et al.* Encapsulating Metal Nanoparticles into a Layered Zeolite Precursor with Surface Silanol Nests Enhances Sintering Resistance. *Angew. Chem. Int. Ed.* 62, e202213361 (2023).
5. Amrute, A. P. *et al.* Mechanochemical Synthesis of Catalytic Materials. *Chem. – Eur. J.* 27, 6819–6847 (2021).
6. Rainer, D. N. & Morris, R. E. New avenues for mechanochemistry in zeolite science. *Dalton Trans.* 50, 8995–9009 (2021).
7. Ryoo, R. *et al.* Rare-earth–platinum alloy nanoparticles in mesoporous zeolite for catalysis. *Nature* 585, 221–224 (2020).
8. Bjelić, A. *et al.* Hydrogenation and hydrodeoxygenation of aromatic lignin monomers over Cu/C, Ni/C, Pd/C, Pt/C, Rh/C and Ru/C catalysts: Mechanisms, reaction micro-kinetic modelling and quantitative structure-activity relationships. *Chem. Eng. J.* 359, 305–320 (2019).
9. Millini, R. & Bellussi, G. Zeolite Science and Perspectives. in *Zeolites in Catalysis: Properties and Applications* (eds. Čejka, J. et al.) 1–36 (The Royal Society of Chemistry, 2017).
10. Baerlocher, Ch. *et al.* Database of Zeolite Structures. https://www.iza-structure.org/databases/.
11. Martínez T., L. M. *et al.* Synthesis and Identification Methods for Zeolites and MOFs. in *Zeolites and Metal-Organic Frameworks* (eds. Blay, V. et al.) 25–52 (Amsterdam University Press, 2018).
12. Valtchev, V. & Mintova, S. Zeolites and MOFs? Dare to Know Them! in *Zeolites and Metal-Organic Frameworks* (eds. Blay, V. et al.) 13–23 (Amsterdam University Press, 2018).

13. Yu, J. Chapter 3 - Synthesis of Zeolites. in *Studies in Surface Science and Catalysis* (eds. Čejka, J. et al.) vol. 168 39–103 (Elsevier, 2007).
14. Bobadilla, L. F. *et al.* Spectroscopic Methods of Characterization for Zeolites and MOFs. in *Zeolites and Metal-Organic Frameworks* (eds. Blay, V. et al.) 53–87 (Amsterdam University Press, 2018).
15. Zhang, H. *et al.* Zeolites in catalysis: sustainable synthesis and its impact on properties and applications. *Catal. Sci. Technol.* 12, 6024–6039 (2022).
16. Corma, A. Inorganic Solid Acids and Their Use in Acid-Catalyzed Hydrocarbon Reactions. *Chem. Rev.* 95, 559–614 (1995).
17. Farrusseng, D. & Tuel, A. Perspectives on zeolite-encapsulated metal nanoparticles and their applications in catalysis. *New J. Chem.* 40, 3933–3949 (2016).
18. Xu, D. *et al.* Encapsulation of Metal Nanoparticle Catalysts Within Mesoporous Zeolites and Their Enhanced Catalytic Performances: A Review. *Front. Chem.* 6, (2018).
19. Wang, Y. *et al.* Zeolite Fixed Metal Nanoparticles: New Perspective in Catalysis. *Acc. Chem. Res.* 54, 2579–2590 (2021).
20. Yilmaz, B. & Müller, U. Catalytic Applications of Zeolites in Chemical Industry. *Top. Catal.* 52, 888–895 (2009).
21. Li, Y. *et al.* Applications of Zeolites in Sustainable Chemistry. *Chem* 3, 928–949 (2017).
22. Bensafi, B. *et al.* The universal zeolite ZSM-5: Structure and synthesis strategies. A review. *Coord. Chem. Rev.* 496, 215397 (2023).
23. Přech, J. *et al.* From 3D to 2D zeolite catalytic materials. *Chem. Soc. Rev.* 47, 8263–8306 (2018).
24. Zhang, Y. *et al.* Nanosponge hierarchical micro-mesoporous MFI zeolites as a high-performance catalyst for the hydroamination of methyl acrylate with aniline. *Microporous Mesoporous Mater.* 341, 112087 (2022).
25. Kim, J.-C. *et al.* Mesoporous MFI Zeolite Nanosponge as a High-Performance Catalyst in the Pechmann Condensation Reaction. *ACS Catal.* 5, 2596–2604 (2015).
26. Shamzhy, M. *et al.* MWW and MFI Frameworks as Model Layered Zeolites: Structures, Transformations, Properties, and Activity. *ACS Catal.* 11, 2366–2396 (2021).

27. Jo, C. *et al.* MFI zeolite nanosponges possessing uniform mesopores generated by bulk crystal seeding in the hierarchical surfactant-directed synthesis. *Chem. Commun.* 50, 4175–4177 (2014).
28. Sun, Q. *et al.* Advances in Catalytic Applications of Zeolite-Supported Metal Catalysts. *Adv. Mater.* 33, 2104442 (2021).
29. Sachtler, W. M. H. Metal clusters in zeolites: an intriguing class of catalysts. *Acc. Chem. Res.* 26, 383–387 (1993).
30. Liu, Q. *et al.* General synthesis for supported single-atom catalysts using hydroxyl nests in zeolites. *J. Mater. Chem. C* 12, 14858–14864 (2024).
31. Chai, Y. *et al.* Noble Metal Particles Confined in Zeolites: Synthesis, Characterization, and Applications. *Adv. Sci.* 6, 1900299 (2019).
32. Zhang, Q. *et al.* Metal Sites in Zeolites: Synthesis, Characterization, and Catalysis. *Chem. Rev.* 123, 6039–6106 (2023).
33. Amiripour, F. *et al.* Nano P zeolite modified with Au/Cu bimetallic nanoparticles for enhanced hydrogen evolution reaction. *Int. J. Hydrog. Energy* 44, 605–617 (2019).
34. Liu, L. & Corma, A. Bimetallic Sites for Catalysis: From Binuclear Metal Sites to Bimetallic Nanoclusters and Nanoparticles. *Chem. Rev.* 123, 4855–4933 (2023).
35. Khalaf, Y. H. *et al.* Bimetallic Catalysts for Isomerization of Alkanes (A Review). *Pet. Chem.* 63, 829–843 (2023).
36. Ou, Z. *et al.* Encapsulating subnanometric metal clusters in zeolites for catalysis and their challenges. *Chem. Eng. J.* 430, 132925 (2022).
37. Wang, N. *et al.* Ultrasmall Metal Nanoparticles Confined within Crystalline Nanoporous Materials: A Fascinating Class of Nanocatalysts. *Adv. Mater.* 31, 1803966 (2019).
38. Fernández-Bertran, J. F. Mechanochemistry: an overview. 71, 581–586 (1999).
39. Colacino, E. *et al.* Advances in Mechanochemistry. *ACS Sustain. Chem. Eng.* 9, 10662–10663 (2021).
40. Majano, G. *et al.* Rediscovering zeolite mechanochemistry – A pathway beyond current synthesis and modification boundaries. *Microporous Mesoporous Mater.* 194, 106–114 (2014).
41. Laurichesse, S. & Avérous, L. Chemical modification of lignins: Towards biobased polymers. *Top. Issue Biomater.* 39, 1266–1290 (2014).

42. Vishtal, A. & Kraslawski, A. Challenges in industrial applications of technical lignins. *Bioresources* 6, 3547–3568 (2011).
43. Sethupathy, S. *et al.* Lignin valorization: Status, challenges and opportunities. *Bioresour. Technol.* 347, 126696 (2022).
44. Chio, C. *et al.* Lignin utilization: A review of lignin depolymerization from various aspects. *Renew. Sustain. Energy Rev.* 107, 232–249 (2019).
45. Bjelić, A. *et al.* Catalytic hydrogenation and hydrodeoxygenation of lignin-derived model compound eugenol over Ru/C: Intrinsic microkinetics and transport phenomena. *Chem. Eng. J.* 333, 240–259 (2018).
46. Becker, J. & Wittmann, C. A field of dreams: Lignin valorization into chemicals, materials, fuels, and health-care products. *Biotechnol. Adv.* 37, (2019).
47. Ulanowska, M. & Olas, B. Biological Properties and Prospects for the Application of Eugenol—A Review. *Int. J. Mol. Sci.* 22, (2021).
48. Sreenavya, A. *et al.* Hydrogenation of Lignin-Derived Phenolic Compound Eugenol over Ruthenium-Containing Nickel Hydrotalcite-Type Materials. *Ind. Eng. Chem. Res.* 59, 11979–11990 (2020).
49. Bunaciu, A. A. *et al.* X-Ray Diffraction: Instrumentation and Applications. *Crit. Rev. Anal. Chem.* 45, 289–299 (2015).
50. Pecharsky, V. K. & Zavalij, P. Y. *Fundamentals of Powder Diffraction and Structural Characterization of Materials*. (Springer, New York, 2009).
51. Morris, R. E. & Wheatley, P. S. Chapter 11 - Diffraction Techniques Applied to Zeolites. in *Studies in Surface Science and Catalysis* (eds. Čejka, J. et al.) vol. 168 375–IX (Elsevier, 2007).
52. Paula, C. In situ solid-state NMR and XRD investigations of structural transformations in crystalline porous solids. (2021).
53. Sotomayor, F. *et al.* Characterization of Micro/Mesoporous Materials by Physisorption: Concepts and Case Studies. *Acc. Mater. Surf. Res.* 3, 34–50 (2018).
54. Thommes, M. Chapter 15 - Textural Characterization of Zeolites and Ordered Mesoporous Materials by Physical Adsorption. in *Studies in Surface Science and Catalysis* (eds. Čejka, J. et al.) vol. 168 495–XIII (Elsevier, 2007).
55. Thommes, M. *et al.* Physisorption of gases, with special reference to the evaluation of surface area and pore size distribution (IUPAC Technical Report). 87, 1051–1069 (2015).

56. Storck, S. *et al.* Characterization of micro- and mesoporous solids by physisorption methods and pore-size analysis. *Appl. Catal. Gen.* 174, 137–146 (1998).
57. Egerton, R. F. The Transmission Electron Microscope. in *Physical Principles of Electron Microscopy: An Introduction to TEM, SEM, and AEM* (ed. Egerton, R. F.) 57–92 (Springer US, Boston, MA, 2005).
58. Van Tendeloo, G. *et al.* Advanced Electron Microscopy for Advanced Materials. *Adv. Mater.* 24, 5655–5675 (2012).
59. Zuo, J.-M. & Spence, J. C. H. *Advanced Transmission Electron Microscopy, Imaging and Diffraction in Nanoscience*. (Springer, New York, 2017).
60. Rose, H. H. Historical aspects of aberration correction. *J. Electron Microsc. (Tokyo)* 58, 77–85 (2009).
61. Geelen, D. *et al.* eV-TEM: Transmission electron microscopy in a low energy cathode lens instrument. *Spec. Issue LEEM-PEEM 9* 159, 482–487 (2015).
62. Egerton, R. F. Choice of operating voltage for a transmission electron microscope. *Low-Volt. Electron Microsc.* 145, 85–93 (2014).
63. Wan, W. *et al.* Transmission electron microscopy as an important tool for characterization of zeolite structures. *Inorg. Chem. Front.* 5, 2836–2855 (2018).
64. Nguyen, K. X. *et al.* Achieving sub-0.5-angstrom–resolution ptychography in an uncorrected electron microscope. *Science* 383, 865–870 (2024).
65. Nellist, P. D. Scanning Transmission Electron Microscopy. in *Springer Handbook of Microscopy* (eds. Hawkes, P. W. & Spence, J. C. H.) 65–132 (Springer, 2007).
66. Cowley, J. M. Scanning Transmission Electron Microscopy. in *Handbook of Microscopy for Nanotechnology* (eds. Yao, N. & Wang, Z. L.) 455–491 (Springer, Boston, MA, 2005).
67. Pennycook, S. J. & Nellist, P. D. *Scanning Transmission Electron Microscopy*. (Springer, New York, NY, 2011).
68. Egerton, R. *Physical Principles of Electron Microscopy: An Introduction to TEM, SEM, and AEM*. *Physical Principles of Electron Microscopy: An Introduction to TEM, SEM, and AEM* (Springer, New York, 2005).
69. Vernon-Parry, K. D. Scanning electron microscopy: an introduction. *III-Vs Rev.* 13, 40–44 (2000).
70. Gleichmann, N. SEM vs TEM. *Analysis & Separations from Technology Networks* https://www.technologynetworks.com/analysis/articles/sem-vs-tem-331262.

71. Bernardi, J. Energy-dispersive X-ray spectroscopy. in *Imaging Modalities for Biological and Preclinical Research: A Compendium, Volume 1: Part I: Ex vivo biological imaging* (eds. Walter, A. et al.) (2021).
72. Chapter 11 Temperature programmed reduction and sulphiding. in *Studies in Surface Science and Catalysis* (eds. Moulijn, J. A. et al.) vol. 79 401–417 (Elsevier, 1993).
73. Bartle, K. D. & Myers, P. History of gas chromatography. *TrAC Trends Anal. Chem.* 21, 547–557 (2002).
74. High Temperature GC Columns for Precise Separation | Phenomenex. https://www.phenomenex.com/techniques/gc-high-temperature?srsltid=AfmBOoq6Pf-rOFXwwWjYl6MNpiMPHBDFwJoZ2Yowtsn4_m-VwOI1Fral.
75. Gas Chromatography: Definition, Working Principle, Components. *GeeksforGeeks* https://www.geeksforgeeks.org/gas-chromatography/.
76. Schindelin, J. *et al.* Fiji: an open-source platform for biological-image analysis. *Nat. Methods* 9, 676–682 (2012).
77. Kurbanova, A. *et al.* Preparation of Fe@MFI and CuFe@MFI composite hydrogenation catalysts by reductive demetallation of Fe-zeolites. *CIS-2021 Young Res.* 390–391, 306–315 (2022).
78. Tan, Q. *et al.* Different Product Distributions and Mechanistic Aspects of the Hydrodeoxygenation of m-Cresol over Platinum and Ruthenium Catalysts. *ACS Catal.* 5, 6271–6283 (2015).
79. Xiaoning, W. *et al.* Effects of Light Rare Earth on Acidity and Catalytic Performance of HZSM-5 Zeolite for Catalytic Cracking of Butane to Light Olefins. *J. Rare Earths* 25, 321–328 (2007).
80. Liu, L. & Corma, A. Metal Catalysts for Heterogeneous Catalysis: From Single Atoms to Nanoclusters and Nanoparticles. *Chem. Rev.* 118, 4981–5079 (2018).